Synthesis and Ligand Non-Innocence of Thiolate-Ligated (N₄S) Iron(II) and Nickel(II) Bis(imino)pyridine Complexes

Leland R. Widger[†], **Yunbo Jiang**[†], **Maxime Siegler**[†], **Devesh Kumar**[⊥], **Reza Latifi**[‖], **Sam P. de Visser**[‖], **Guy N.L. Jameson**[‡], and **David P. Goldberg**[†,*]

[†]Department of Chemistry, The Johns Hopkins University, 3400 North Charles Street, Baltimore, MD 21218, USA [‡]Department of Chemistry & MacDiarmid Institute for Advanced Materials and Nanotechnology, University of Otago, PO Box 56, Dunedin 9054, New Zealand [‖]Manchester Institute of Biotechnology and School of Chemical Engineering and Analytical Science, The University of Manchester, 131 Princess Street, Manchester M1 7DN, United Kingdom [⊥]Department of Applied Physics, School for Physical Sciences, Babasaheb Bhimrao Ambedkar University, Vidya Vihar, Rae Bareilly Road, Lucknow (U. P.) 226 025, India

Abstract

The known iron(II) complex [Fe^{II}(LN$_3$S)(OTf)] (**1**) was used as starting material to prepare the new biomimetic (N$_4$S(thiolate)) iron(II) complexes [Fe^{II}(LN$_3$S)(py)](OTf) (**2**) and [Fe^{II}(LN$_3$S)(DMAP)](OTf) (**3**), where LN$_3$S is a tetradentate bis(imino)pyridine (BIP) derivative with a covalently tethered phenylthiolate donor. These complexes were characterized by X-ray crystallography, UV-vis, ^{1}H NMR, and Mössbauer spectroscopy, as well as electrochemistry. A nickel(II) analogue, [Ni^{II}(LN$_3$S)](BF$_4$) (**5**), was also synthesized and characterized by structural and spectroscopic methods. Cyclic voltammetric studies showed **1** – **3** and **5** undergo a single reduction process with $E_{1/2}$ between –0.9 to –1.2 V versus Fc$^+$/Fc. Treatment of **3** with 0.5% Na/Hg amalgam gave the mono-reduced complex [Fe(LN$_3$S)(DMAP)]^0 (**4**), which was characterized by X-ray crystallography, UV-vis, EPR (g = [2.155, 2.057, 2.038]) and Mössbauer (= 0.33 mm s^{-1}; E$_Q$ = 2.04 mm s^{-1}) spectroscopies. Computational methods (DFT) were employed to model complexes **3** – **5**. The combined experimental and computational studies show that **1** – **3** are 5-coordinate, high-spin (S = 2) Fe^{II} complexes, whereas **4** is best described as a 5-coordinate, intermediate-spin (S = 1) Fe^{II} complex antiferromagnetically coupled to a ligand radical. This unique electronic configuration leads to an overall doublet spin (S$_{total}$ = ½) ground state. Complexes **2** and **3** are shown to react with O$_2$ to give S-oxygenated products, as previously reported for **1**. In contrast, the mono-reduced **4** appears to react with O$_2$ to give a mixture of S- and Fe-oxygenates. The nickel(II) complex **5** does not react with O$_2$, and even when the mono-reduced nickel complex is produced, it appears to undergo only outer-sphere oxidation with O$_2$.

Introduction

Thiolate-ligated nonheme iron sites play key roles in biology, exhibiting diverse structural features as well as contributing to a wide range of reactivity.[1–7] The mononuclear, thiolate-

---

ligated nonheme iron enzymes superoxide reductase,[8–12] nitrile hydratase,[13–15] and cysteine dioxygenase (CDO)[16–23] utilize single iron sites coordinated in mixed N/S ligand environments. Work by some of us has focused on the preparation of synthetic analogs of these sites, including some of the first structural and functional models of CDO.[1,24–33] A bis(imino)pyridine (BIP) ligand scaffold was employed, leading to the synthesis of $Fe^{II}(LN_3S)$ complexes that mimicked certain structural and functional features of CDO.[24,25] The key thiolate donor was incorporated into these complexes by either covalent attachment to the BIP backbone, or by addition of an exogenous phenylthiolate (PhS$^-$) ligand to the iron(II) center, yielding $Fe^{II}(N_3S)$ complexes in both cases. These complexes were among the first mononuclear thiolato-iron(II) complexes to selectively react with O_2 to give S-oxygenated products, reproducing the gross reactivity of the enzymatic system. However, the Cys-bound iron(II) form of CDO contains an iron center held in an (N_4S) donor set, comprised of 3 His ligands and one Cys substrate chelated through both the amino and sidechain S groups. Thus we are currently interested in the design and synthesis of $Fe^{II}(N_4S)$ complexes in which a fourth neutral N donor is included in the first coordination sphere to more closely match the active site of CDO prior to S-oxygenation.

Herein we describe the synthesis, spectroscopic characterization and O_2 reactivity of a new series of $Fe^{II}(N_4S)$ complexes (Figure 1) that contain a covalently-linked, BIP-derived ligand providing an N_3S(thiolate) donor set (LN$_3$S$^-$), and a fourth N donor derived from exogenous pyridine derivatives. The general synthetic strategy was to incorporate a fourth N donor without the need for covalent modification of the BIP backbone. This strategy proved productive, and the new iron(II) complexes $[Fe^{II}(LN_3S)(py)](OTf)$ (**2**) and $[Fe^{II}(LN_3S)(DMAP)](OTf)$ (**3**) were synthesized and characterized by X-ray crystallography, NMR, electrochemistry, Mössbauer spectroscopy and density functional theory (DFT) calculations. A nickel(II) analog, $[Ni^{II}(LN_3S)](BF_4)$ (**5**), was also prepared for comparative spectroscopic and reactivity studies.

The BIP platform is also well known to behave as a non-innocent ligand, allowing for the storage of multiple reducing equivalents on the ligand backbone. The BIP framework has been shown to accept up to three electrons, which are stabilized by delocalization over the conjugated ligand scaffold. [34–45] However, the reduced analogs of these BIP complexes are generally restricted to derivatives in which only minor changes to the aryl substitution patterns on the imino positions have been made, with no major modification of the chelating abilities of the BIP framework. There is significant interest in the development of non-innocent, polydentate ligands for their use as redox-active partners in combination with metal ions to assist with various chemical transformations such as the reduction of small-molecules (e.g. CO_2, N_2) and other redox reactions. With the thiolate-modified LN$_3$S system in hand, we thus wanted to determine if it could also function as a non-innocent ligand, perhaps stabilizing one or more reducing equivalents across the ligand backbone. A question to be addressed concerns the influence of the additional, covalently-linked phenylthiolate arm on the stability, spin delocalization, and spectroscopic and redox properties of possible (multi)reduced ligand-metal complexes. It is also of interest to determine if multiple reducing equivalents stored on both the ligand and the metal can be employed together for the activation of O_2, and how this combination will affect subsequent S- or metal-based oxygenation steps.

The new complexes $[Fe^{II}(LN_3S)(py)]OTf$ (**2**), $[Fe^{II}(LN_3S)(DMAP)]OTf$ (**3**) and $[Ni^{II}(LN_3S)]BF_4$ (**5**) were shown to accept a single electron to give the respective mono-reduced products. In one case, successful crystallization of the mono-reduced species was achieved, and the structure of $[Fe(LN_3S)(DMAP)]^0$ (**4**) was obtained by X-ray crystallography. A detailed experimental and computational (DFT) investigation into the electronic and structural properties of **4**, as well as the other mono-reduced analogs, was

conducted, revealing a number of insights regarding the interplay between the structures and the electronic configurations of these complexes. The influence of the stong field thiolate donor, the extent of non-innocence in the BIP ligand, and the oxidation and spin state of the metal center are addressed. A major finding from these studies is that complex **4**, based on experimental and computational results, is a mono-reduced bis(imino)pyridine complex with an intermediate-spin iron(II) center coupled with a stable ligand-based radical.

The O_2 reactivity of these complexes was also examined, and for the starting iron(II) complexes **2** and **3**, selective S-oxygenation to give sulfonato (RSO_3^-) products was observed, as seen previously for [$Fe^{II}(LN_3S)(OTf)$] (**1**).[24] In contrast, the mono-reduced complex **4** reacts with O_2, leading to a mixture of products that suggest both Fe- and S-oxygenation readily occur for this mono-reduced species. However, both the Ni^{II} complex **5**, and its mono-reduced analog, do not exhibit any S- or metal-based oxygenation in the presence of O_2 even after prolonged reaction times. This lack of reactivity is in contrast to the iron analogs, as well as some nickel-thiolate complexes that do react with O_2 to give S-oxygenated sulfinato and sulfonato products, although these reactions can be sluggish.[46–54]

Experimental

General Procedures

All reagents were purchased from commercial vendors and used without further purification unless noted otherwise. All reactions were carried out under an atmosphere of N_2 inside a glovebox or under Ar by standard Schlenk and vacuum line techniques. UV-visible spectra were recorded on an Agilent 8453 photodiode array spectrophotometer. Electron paramagnetic resonance (EPR) spectra were obtained on a Bruker EMX EPR spectrometer controlled with a Bruker ER 041 X G microwave bridge at 15 K. The EPR spectrometer was equipped with a continuous-flow liquid He cryostat and an ITC503 temperature controller made by Oxford Instruments, Inc. NMR was performed on a Bruker Avance 400 MHz FT-NMR spectrometer at 25 °C. Elemental analysis was performed by Atlantic Microlab Inc., Norcross, GA. LDI-ToF mass spectra were obtained using a Bruker Autoflex III Maldi ToF/ToF instrument (Billerica, MA). Samples were dissolved in CH_2Cl_2 and deposited on the target plate in the absence of any added matrix. Samples were irradiated with a 355 nm UV laser and mass-analyzed by ToF mass spectrometry in the reflectron mode. $Fe^{II}(LN_3S)(OTf)$ (**1**) was prepared according to literature procedure.[24] ^{57}Fe Mössbauer spectra were recorded on a Mössbauer spectrometer from SEE Co. (Science Engineering & Education Co., MN) equipped with a closed cycle refrigerator system from Janis Research Co. and SHI (Sumitomo Heavy Industries Ltd.). Approximately 10 mg of sample was placed in a custom sample holder made from Teflon and specifically designed for solid samples. Data were collected in constant acceleration mode in transmission geometry with an applied field of 47 mT parallel to the -rays. The zero velocity of the Mössbauer spectra refers to the centroid of the room temperature spectrum of a 25 μm metallic iron foil. Analysis of the spectra was conducted using the WMOSS program (SEE Co., formerly WEB Research Co., Edina, MN).

Computational Methods

Density functional theory calculations were performed on complexes **3** – **5** using methods and procedures we have tested and calibrated previously.[55,56] The complexes were calculated in several possible spin states. The spin state ordering of transition metal complexes can be dependent on the DFT functional chosen, and thus we tested several different methods for our calculations. In an initial set of calculations, the unrestricted hybrid density functional method B3LYP was used in combination with an LACVP basis set on the metal and 6-31G on the rest of the atoms (basis set B1) for geometry optimizations and frequencies.[57–59] Optimized structures were employed as the starting point for single

point calculations using (*a*) the LACV3P+ basis set on the metal and 6-311+G* on the rest of the atoms; (*b*) the M06/B1 method;[60] (*c*) B3LYP/B1 with the polarized continuum model with a dielectric constant of = 5.7. In a second set of calculations we used the unrestricted BP86 density functional method[61,62] in combination with an LACV3P+ basis set on the metal and 6-311+G* on the rest of the atoms; basis set B2. Full geometry optimizations were run in *Jaguar* 7.6 and followed by a frequency calculation using these methods.[63] Single point calculations with dispersion corrected DFT were performed as proposed by Schwabe and Grimme,[64] however, this had a negligible effect on the spin state ordering and relative energies.

Synthesis of [Fe^{II}(LN$_3$S)(py)]OTf (2)

Crystalline [Fe^{II}(LN$_3$S)(OTf)] (**1**) (100 mg, 0.16 mmol) was dissolved in CH_2Cl_2 and pyridine (15 µL, 0.19 mmol) was added. After stirring for 2 h, the solution was filtered through celite. Slow vapor diffusion of diethyl ether or layering with pentane gave the desired product as dark brown plates suitable for X-ray diffraction in 97% yield (110 mg). ^1H NMR (CD$_2$Cl$_2$): 107.0, 95.4, 91.6, 45.2, 13.1, 11.6, 3.1, 1.3, −4.1, −10.3, −16.2, −30.4. LDIMS (+): *m/z* 484.2 ([**2** − py − OTf]$^+$). *Anal. Calc.* for Fe^{II}(L$_3$NS)(py)(OTf) •CH$_2$Cl$_2$ (C$_{34}$H$_{37}$Cl$_2$F$_3$FeN$_4$O$_3$S$_2$): C, 51.20; H, 4.68; N, 7.02. Found: C, 51.21; H, 4.88; N, 7.67.

Synthesis of [Fe^{II}(LN$_3$S)(DMAP)]OTf (3)

Crystalline [Fe^{II}(LN$_3$S)(OTf)] (**1**) (110 mg, 0.17 mmol) was dissolved in CH_2Cl_2 and DMAP (25 mg, 0.21 mmol) was added. After stirring for 2 h, the solution was filtered through celite. Slow vapor diffusion of diethyl ether or layering with pentane gave **3** as black plates suitable for X-ray diffraction in 95% (125 mg). ^1H NMR (CD$_2$Cl$_2$): 128.0, 102.4, 92.8, 37.6, 19.4, 10.4, 8.4, 3.1, 1.4, −4.9, −7.7, −10.4, −13.7, −22.8. LDIMS (+): *m/z* 484.2 ([**3** − DMAP − OTf]). *Anal. Calc.* for Fe^{II}(LN$_3$S)(DMAP)(OTf) (C$_{35}$H$_{40}$F$_3$FeN$_5$O$_3$S$_2$): C, 55.63; H, 5.34; N, 9.27. Found: C, 55.37; H, 5.29; N, 9.07.

Synthesis of [Fe^{II}(LN$_3$S)(DMAP)]•2Et$_2$O (4•2Et$_2$O)

Crystalline [Fe^{II}(LN$_3$S)(DMAP)](OTf) (**3**) (125 mg, 0.17 mmol) was combined with 1.5 equiv of 0.5% Na/Hg amalgam (6.0 mg Na^0, 1.15 g Hg) and suspended in 5 mL of Et$_2$O. Upon stirring, the insoluble starting material (**3**) slowly dissolves into solution as it reacts, giving a dark green/brown solution. After stirring for 2 h, the reaction mixture was filtered through celite, layered with pentane, and placed in the freezer for several days, giving **4•2Et$_2$O** as dark brown crystals suitable for X-ray diffraction (38 mg, 37% yield). UV-vis (nm): 566, 625, 785 (= 890 M$^{−1}$cm$^{−1}$). ^1H NMR (THF-d_8): 95.7, 33.8, 24.7, 5.8. ^{19}F NMR (THF-d_8): −79.3. EPR: g = 2.155, 2.057, 2.038. Mössbauer: $_{L=R}$ = 0.8 mm s$^{−1}$, = 0.33 mm s$^{−1}$, E_Q = 2.04 mm s$^{−1}$. *Anal. Calc.* for [**4** + Et$_2$O + 0.25 NaOTf] (C$_{38.25}$H$_{50}$F$_{0.75}$FeN$_5$Na$_{0.25}$O$_{1.75}$S$_{1.25}$): C, 63.48; H, 6.96; N, 9.68. Found: C, 62.85; H, 6.74; N, 9.73. Crystalline samples of **4•2Et$_2$O** co-precipitate with a small amount of white solid impurity that could not be separated from **4•2Et$_2$O**. The impurity was identified as NaOTf by ^{19}F NMR (Figure S2). Inclusion of 0.25 equiv of NaOTf was necessary to obtain a good fit for elemental analysis.

Synthesis of [Ni^{II}(LN$_3$S)]BF$_4$ (5)

An amount of 2-(O=CMe)-6-(2,6-(^{i}Pr2-C$_6$H$_3$N=CMe)-C$_5$H$_3$N (50 mg, 0.155 mmol) and Ni^{II}(BF$_4$)$_2$•6H$_2$O (55.4 mg, 0.163 mmol) was suspended in EtOH (5 mL) and heated at 80 °C for 30 min. The solids slowly dissolved to give a deep green solution, and then a solution of 2-aminothiophenol (17 µL, 0.155 mmol) and triethylamine (22 µL, 0.155 mmol) in EtOH (1 mL) was added to the reaction mixture. The reaction was allowed to stir at 80 °C for 24 h

before being cooled to room temperature and concentrated. The resulting solid residue was brought into a glovebox where it was redissolved in a minimum amount of CH_2Cl_2 and filtered through Celite. Slow vapor diffusion of diethyl ether into the filtrate yielded 96 mg (94% yield) of **5** as dark red crystals suitable for X-ray analysis, together with colorless crystals of $Et_3NH \bullet BF_4$. Samples for elemental analysis were prepared by manual separation of crystals of **5** from the colorless $Et_3NH \bullet BF_4$ crystals. ^{1}H NMR (CD_2Cl_2): 8.30 (br, 1H), 7.89 (br, 2H), 7.35 (t, 1H), 7.22 (d, 2H), 7.09 (d, 1H), 6.92 (t, 1H), 6.82-6.72 (m, 2H), 3.18 (br), 2.69 (s, 3H), 2.14 (s, 3H), 2.14 (s, 3H), 1.50 (d, 6H), 1.33 (br), (1.17 (d, 6H). LDIMS (+): *m/z* 488.3 [**5**-BF_4]$^+$. *Anal. Calc.* for [Ni^{II}(L_3NS)](BF_4)•CH_2Cl_2] ($C_{28}H_{32}BCl_2F_4N_3NiS$): Predicted: C, 51.03; H, 4.89; N, 6.38. Found: C, 51.28; H 4.76; N, 6.66.

O$_2$ reactivity

Reactions of **2**, **3** and **5** with excess O_2 were conducted as previously reported for **1** in CH_2Cl_2.[24] The one-electron reduced complexes were reacted with O_2 by freshly preparing solutions of **4** or reduced **5** via Na/Hg amalgam in Et_2O followed by filtration through Celite, as described for the synthesis of **4**. Reaction mixtures following O_2 addition were then analyzed directly by LDI-MS.

Results and Discussion

Synthesis of Iron(II) and Nickel(II) Complexes

The synthesis of the unsymmetrical, thiolate-ligated complex [Fe^{II}(LN_3S)(OTf)] (**1**) was accomplished by reacting the imino-ketone precursor[65] 2-(O=CMe)-6-(2,6-(^{i}Pr$_2$-C_6H_3N=CMe)-C_5H_3N with the commercially available 2-aminothiophenol and Fe(OTf)$_2$ in a metal-assisted template reaction as previously described.[24] We sought to determine if this complex could be used as a precursor to generate Fe^{II} complexes with biologically relevant [N$_4$S] donor sets via substitution at the OTf$^-$ position. Displacement of the OTf$^-$ ligand in **1** was an attractive route when compared to the more challenging strategy involving multi-step organic synthesis to produce covalently linked N$_4$S-donating ligands.[26,66–68] Addition of one equivalent of either pyridine or *N,N'*-dimethylaminopyridine (DMAP) to dark red-purple **1** in CH_2Cl_2 at room temperature does not result in any color change. However, vapor diffusion of diethyl ether into the reaction mixture after stirring for 2 h afforded single crystals as dark brown plates of the pyridine-ligated [Fe^{II}(LN_3S)(py)](OTf) (**2**), and black plates in the case of the DMAP-ligated [Fe^{II}(LN_3S)(DMAP)](OTf) (**3**). These crystals yielded the X-ray structures of **2** and **3** (Figures 2 and 3) (vide infra), confirming that the OTf$^-$ anion was displaced by the pyridine derivatives. For large-scale preparations of **2** and **3**, layering of pentane was used in place of vapor diffusion of Et_2O to give both **2** and **3** in high yield.

The synthesis of the Ni^{II} analog of **1** was also targeted for comparison of spectroscopic features and its reactivity toward O_2. The use of Ni^{II}(BF_4)$_2$ in place of Fe^{II}(OTf)$_2$ in Scheme 1 results in a dark green solution. Vapor diffusion of Et_2O afforded dark red crystals together with clusters of large colorless needles. The red crystals were separated by hand and analyzed by X-ray crystallography revealing the Ni^{II} complex [Ni^{II}(LN_3S)](BF_4) (**5**, see Figure 4). The colorless crystals were presumed to be $Et_3NH^+BF_4^-$, the expected byproduct of the template reaction. Peaks corresponding to $Et_3NH^+BF_4^-$ were confirmed in the ^{1}H NMR of **5** (Figure 6). The co-precipitation of $Et_3NH^+BF_4^-$ could not be avoided even upon successive recrystallizations, and therefore it was necessary to isolate complex **5** by manual separation of crystalline material for elemental analysis and further reactivity studies.

X-ray Structures of Iron(II) and Nickel(II) Complexes

The X-ray structures for the iron(II) complexes $[Fe^{II}(LN_3S)(py)](OTf)$ (**2**) and $[Fe^{II}(LN_3S)(DMAP)](OTf)$ (**3**) are shown in Figures 2 and 3. Selected bond distances and angles are given in Tables 1 and 2. The structures reveal that the triflate ligand has been displaced in each case by the heterocyclic N donor to afford the 5-coordinate $Fe^{II}(N_4S(thiolate))$ products. There is a clear preference for forming the 5-coordinate complexes over the 6-coordinate species, in which the OTf^- would be retained in the first coordination sphere. The Fe-N distances of 2.073(5) – 2.196(5) Å for **2** and 2.0667(14) – 2.2179(15) Å for **3** are indicative of high-spin ($S = 2$) Fe^{II} complexes. The pyridine-derived Fe-N bonds are shorter than the imine nitrogen-to-iron distances in both **2** and **3**, whereas the Fe-S bonds are nearly identical. There is minimal effect of substitution of the *para* position of the pyridine derivatives on the bond lengths in **2** and **3**. An analysis of the bond angles for **2** and **3** and their values (**2**: = 0.15; **3**: = 0.18; where = 0 for square pyramidal and = 1 for trigonal bipyramidal)[69] show that in both cases the Fe^{II} ions are held in a distorted square pyramidal geometry, with the pyridine derivatives occupying the axial position. The molecular structure of **1** has been reported,[24] and select bond distances are reproduced in Table 1. The Fe-N distances are very similar to those found in **2** and **3**, whereas the Fe-S distance appears slightly shorter. Complex **1** exhibits a more idealized square pyramidal geometry than **2** or **3**, with = 0.12, and a comparison of the values for **1** – **3** reveals that the geometry becomes more distorted from square pyramidal with increasing axial ligand donor strength ($_{(OTf)}$ = 0.12 < $_{(py)}$ = 0.15 < $_{(DMAP)}$ = 0.18). In all three complexes **1** – **3**, the pyridine diimine backbone remains planar, while the ferrous ion sits 0.276 Å above the N_3 plane for **1**, but less out of plane for **2** (0.116 Å) and **3** (0.200 Å). In addition, the thiolate donor never sits in the ideal equatorial position, but rather lies well below the N_3 plane. For **1** and **2** the N_{plane}–S distance is 0.824 and 1.18 Å, respectively, while for **3** it is significantly more distorted with $d(N_{plane}$–S) = 1.8 Å. The C_{imine}-N and C_{imine}-C_{ipso} bond distances for the ligand are similar for complexes **1**–**3** (Table 1), and are consistent with a neutral-ligand bis(imino)pyridine backbone (LN_3S^-).[34,43]

The X-ray structure for the Ni^{II} complex $[Ni^{II}(LN_3S)](BF_4)$ (**5**) is shown in Figure 4. Selected bond distances and angles for **5** are given in Table 3. The molecular structure of **5** shows a square planar geometry for the Ni^{II} ion. The observed Ni-N distances are 1.8151(14) – 1.9159(15) Å, and are somewhat shorter (~0.1 – 0.4 Å) than other BIP-derived nickel(II) complexes.[45,70–73] The Ni-S distance of 2.1386(5) Å is significantly shorter than the Fe^{II}–S distances seen for **1** – **3**, as are the Ni–N distances. The bond angles about the Ni^{II} center deviate slightly from the idealized square-planar geometry (82.44 – 102.37°), likely due to the constraints imposed by the three 5-membered chelate rings. The Ni^{II} ion and S atom sit directly in the plane of the bis(imino)pyridine ligand as seen by Ni–N_3(plane) and S-N_3(plane) distances of 0.030 Å and 0.082 Å, respectively. This structure contrasts those found for **1** – **3**, where both the metal ion and sulfur donor lie significantly out of the bis(imino)pyridine plane for these 5-coordinate complexes.

NMR Spectroscopy

The paramagnetic ^1H NMR spectra for complexes **1** – **3** in CD_2Cl_2 are shown in Figure 5. Each complex exhibits sharp, paramagnetically shifted peaks over a broad range (130 to −30 ppm), indicative of high-spin ($S = 2$) Fe^{II} complexes. Detailed ^1H NMR assignments have been made for bis(imino)pyridine iron(II) complexes that carry the same aryl imino substituents.[34,65,74,75] These data can be used as a guide for interpreting the spectra for **1** – **3**, although the unsymmetrical structures of **1** – **3** make their ^1H NMR patterns too difficult to definitively assign. For all three complexes, the downfield region (130 to 80 ppm) contains three sharp peaks, with the exception of **3**, in which the most downfield resonance at 130 ppm is significantly broadened. In comparison to symmetrical $(BIP)FeX_2$ complexes,

two of the three resonances in this region can be assigned to the *meta* and *para* pyridyl backbone protons, with the most intense resonance (82.8, 95.4, and 92.8 ppm for **1 – 3**, respectively) likely arising from the *meta* protons that are apparently not split in the local symmetry. We tentatively assign the third resonance to a proton on the phenylthiolate ring. No peaks appear in the spectrum for **1** between 80 and 20 ppm, whereas complex **2** shows a broad peak at 45.2 ppm and complex **3** exhibits a sharp peak at 37.6 ppm and a broad feature at 43.5 ppm. The latter peaks for **2** and **3** can be assigned to the axial pyridine ligands, which are absent in **1**. This assignment was confirmed by the generation in situ of **2** with the addition of one equiv of pyridine-d_5 to **1**. As seen in Figure 5, the spectrum for deuterated **2**-d_5 is a good match for **2** except for the disappearance of the resonance at 45.2 ppm. The broadness of the py peak and the absence of distinct signals for the *ortho*, *meta* and *para* protons suggest that the py ligand in **2** is labile on the NMR timescale. In contrast two peaks are seen for **3** in the region of the axial DMAP donor, and one is relatively sharp, suggesting that DMAP is significantly less labile than py, and consistent with it being a more strongly donating py derivative. Further upfield, the diisopropyl methyl groups can easily be assigned to the intense singlets between 1.20 – 1.36 ppm for **1 – 3**, and the peaks found from −14 to −16 ppm are assigned to the *para* C–H on the iPr$_2$Ph substituent based on earlier work.[34,65,74,75] The upfield resonances at −21.9, −30.3, and −22.8 ppm for **1 – 3**, respectively, likely arise from the isopropyl methine protons.

The ^{1}H NMR spectrum of the diamagnetic Ni(II) complex **5** is shown in Figure 6. The peaks for the pyridyl protons are seen at   8.30 and 7.88, and the diisopropylphenyl peaks are assigned to   7.35 (t, 1H) and 7.22 (d, 2H). Other peaks in the aromatic region include   7.09 (d, 1H), 6.92 (t, 1H), and overlapping peaks at 6.79 (d, 1H) and 6.75 (t, 1H), which can be attributed to the phenylthiolate ring. The peaks found at 3.18 and 1.33 ppm come from a small amount of Et$_3$NH$^+$BF$_4^-$ impurity (vide supra), and the peak at 3.18 ppm likely masks the isopropyl methine C–H peaks for **5**. The ketimine CH$_3$ resonances are located at   2.70 (s, 3H) and 2.14 (s, 3H). There are two distinct isopropyl CH$_3$ peaks found at   1.50 (d, 6H) and 1.17 (d, 6H), indicating restricted rotation of the diisopropylphenyl substituent about the N$_{imino}$–C$_{ipso}$ bond.

Electrochemistry

Cyclic voltammetry of the iron(II) and nickel(II) complexes was measured to gain insights regarding the influence of the exogenous py derivatives and covalently tethered phenylthiolato donor on the redox properties of these complexes. The cyclic voltammograms for compounds **1**, **2**, **3** and **5** are shown in Figure 7. The triflate complex **1** and the pyridine complex **2** exhibit quasireversible waves at $E_{1/2}$ = −1.1 V, while the DMAP complex **3** reveals a more negative $E_{1/2}$ = −1.2 V. No other obvious redox processes for these complexes are present within the solvent window for CH$_3$CN. The fact that the $E_{1/2}$ values for **1** and **2** are the same suggest that the axial pyridine donor in **2** does not exhibit any influence on the redox potential, but is also consistent with the pyridine ligand dissociating to some extent in solution as indicated by the NMR data. Substitution of py for DMAP does have a clear impact, shifting the redox potential by ~100 mV more negative in **3** as compared to **2**. This result is consistent with DMAP being a more strongly donating ligand than unsubstituted pyridine. The nickel(II) complex is the easiest to reduce in the series, with $E_{1/2}$ = −0.9 V.

Non-innocent BIP ligands have been shown previously to undergo up to three sequential reductions in which the electrons are delocalized over the BIP backbone.[34–45] The negative $E_{1/2}$ values for **1 – 3** are consistent with ligand-based reduction, and covalent attachment of the phenylthiolate group exerts a strong influence on the redox properties in comparison to other BIP complexes.[25] The non-thiolate-ligated BIP complexes typically show two

reversible reduction waves, whereas **1 – 3** exhibit only one reduction process, suggesting that the next reduction for **1 – 3,** if it exists, lies outside the solvent window. Similarly, the nickel(II) analogue **5** exhibits only one redox process at −0.9 V, which is within the range of ligand-based reductions for the iron complexes, but is more positive by 200 mV. These data show that the BIP-derived ligand of the Ni^{II} complex **5** is significantly easier to reduce than **1**–**3**.

One-Electron Reduction of the Iron(II) and Nickel(II) Complexes

A summary of the possible redox transformations for the phenylthiolate-appended $[M(LN_3S)(L)]^+$ complexes are shown in Scheme 2. The CV data for **1 – 3** and **5** each show well-separated, quasi-reversible reduction waves, indicating that one-electron-reduced complexes should be synthetically accessible. The lack of a second reduction process suggests that the one-electron-reduced complexes can be isolated without the complication of forming two-electron-reduced species, in contrast to other BIP complexes.[39] A number of methods have been employed to reduce $M^{n+}(BIP)$ complexes, including treatment with aluminum/lithium alkyl reagents, $NaBEt_3H$, KC_8, and Na/Hg amalgam.[35,70,76,77] The latter method was a convenient choice for the controlled reduction of the thiolate-ligated complexes described here.

Reduction of the DMAP complex **3** was accomplished by stirring a suspension of **3** in Et_2O over a slight excess of 0.5% Na/Hg amalgam, affording the one-electron-reduced $[Fe(LN_3S)(DMAP)]^0$ (**4**) as shown in Scheme 3. The progress of the reaction is easily followed by the colorless ethereal suspension of **3** converting to a deep green, homogeneous solution. The UV-vis spectrum following the Na/Hg reduction is shown in Figure 8, where the solvent is THF instead of Et_2O to maintain the solubility of **3**. Distinct features appear at 566, 625, and 785 nm that are indicative of **4**. It should be noted that solutions of **4** in either THF or Et_2O are extremely air-sensitive, and will decompose upon prolonged standing even at −35 °C in a drybox freezer, as seen by spontaneous conversion of dark green solutions of **4** to a brown precipitate. Crystals for X-ray diffraction can be grown from layering of pentane into Et_2O at −35 °C, but the crystals must be obtained within 48 hours or decomposition occurs and no crystalline product will form. Crystalline **4** is also difficult to isolate outside of the mother liquor without further decomposition. Attempts to scale up the reaction failed to give crystalline product, instead leading to more rapid decomposition.

A number of reduced Fe(BIP) complexes have been reported, most involving doubly-reduced species relative to the M^{II} complexes analogous to **1 – 3**. However, a few examples of mono-reduced and triply-reduced, Fe(BIP) complexes have been described.[37–39] The mono-reduced Fe(BIP) complexes were prepared by either reduction of iron(II) starting materials (e.g. $[^{iPr}BIP)Fe^{II}Cl_2] + e^-$ $[(^{iPr}BIP)FeCl]^0$), or oxidation of doubly-reduced (formally Fe^0) Fe(BIP) complexes (e.g. $[(^{iPr}BIP)Fe(N_2)]^0$ $[(^{iPr}BIP)Fe(OEt_2)]^+ + e^-$), and in both cases yield 4-coordinate iron complexes.[37–39] The 5-coordinate complexes $[(^{iPr}BIP)Fe(Br)(THF)]$ and $[(^{iPr}BIP)Fe(CO)_2]^+$, were prepared via one-electron oxidation of their respective doubly-reduced precursors, while $[(^{Et}BIP)Fe(Cl)(Et_2O)]$ was prepared by reduction of the starting material.[37,40,78] However, the doubly-reduced species in general are more easily obtained than the mono-reduced analogs, and careful stoichiometric control must be used to synthesize mono-reduced complexes. In contrast, the putative doubly-reduced analog of **3** is not accessible as seen by electrochemistry, and thus reduction of **3** leads to the selective isolation of a rare 5-coordinate, mono-reduced complex.

Attempted reductions of the iron(II) complexes **1** and **2** suspended in Et_2O led to similar deep green solutions as seen for **4**, but the products were highly soluble even in mixtures with pentane, and crystals could not be isolated. The nickel(II) complex **5**, which is

insoluble in Et_2O, reacts similarly with Na/Hg amalgam to give a homogenous bright green solution which presumably contains the mono-reduced nickel analog. This product was also highly soluble and could not be crystallized, but provides a useful comparison to iron-containing **4**, and therefore it was prepared in situ from **5** and characterized by EPR spectroscopy (vide infra).

X-ray Structure of Mono-Reduced [Fe(LN₃S)(DMAP)]⁰ (4)

The crystal structure of **4** (Figure 9) shows an overall neutral iron complex with no additional counterions. Charge balance therefore indicates that this complex is the one-electron-reduced analog of the cation of **3**. The DMAP is retained in the axial position and together with the LN_3S ligand gives a 5-coordinate iron center. Selected bond distances and angles are given in Tables 1 and 2. The Fe and S atoms in **4** have moved toward the equatorial plane of the bis(imino)pyridine backbone (Fe–N_3(plane) = 0.254 Å and S-N_3(plane) = 0.411 Å) as compared to **3**. This flattening of the geometry around the iron center is characterized by a change in tau value from τ = 0.18 for **3** to τ = 0.08 for **4**. There is a significant shortening of the Fe-N and Fe-S bonds for LN_3S, with the Fe-S bond decreasing by 0.1 Å and the Fe-N bonds decreasing by 0.3 Å. These changes are opposite to what would be expected for a metal-centered reduction to give a formal high-spin iron(I) complex, and are more consistent with ligand-based reduction.

It has been shown that the C–C and C–N bond distances in BIP complexes are indicative of ligand reduction and an analysis of ligand backbone distances is essential when assigning the locus of reduction in these complexes.[37–43] To gain insight into the electronic structure of **4**, it is useful to compare metrical parameters with other structurally characterized 5-coordinate mono-reduced complexes reported in the literature. The complexes [Fe(^{iPr}BIP)(Br)(THF)][78] and [Fe(^{Et}BIP)(Cl)][40] exhibit similar C_{imine}-N_{imine}, C_{imine}-C_{ipso}, and C_{ipso}-$C_{pyridyl}$ bond distances in the BIP backbone that are consistent with one-electron ligand reduction. In contrast, [Fe(^{iPr}BIP)(CO)₂](BAr$^F_4$)[37], another mono-reduced complex, has bond distances closer to a non-reduced BIP ligand and has been assigned as an iron(I) complex. The critical metrical parameters for **4** are highlighted in the structural fragments shown in Figure 10, in which **4** can be compared with its non-reduced precursor **3**. The C-N_{imine} and C-$N_{pyridyl}$ bonds are elongated, while the C_{imine}-C_{ipso} bonds are shortened in **4** as compared to **3**. These changes in the ligand backbone clearly point to the complex undergoing ligand-based reduction upon conversion of **3** to **4**. A careful comparison of the bond distances in **4** to those reported in the literature suggests the ligand in **4** is similar to a two-electron reduced BIP ligand. However, **4** would need to be formulated as an Fe^{III} complex with a doubly-reduced $(LN_3S)^{3-}$ ligand, which is unlikely given that iron(III) complexes are often not stable in the presence of monoanionic thiolate donors. Further evidence from Mössbauer spectrosocopy and DFT calculations point to **4** as being an iron(II) complex with a one-electron reduced ligand (vide infra). The phenylthiolate-appended LN_3S ligand appears capable of behaving as a non-innocent ligand by accommodating a reducing equivalent delocalized over the BIP backbone.

EPR Spectroscopy

Further information regarding the electronic structure of the mono-reduced **4** was obtained by EPR spectroscopy. Crystalline **4** was dissolved in Et_2O and EPR data were recorded at 15 K. A nearly axial EPR spectrum was observed, and a good simulation was obtained for an S = ½ system with g values of 2.155, 2.057, and 2.038 (Figure 11). The S = ½ ground state could arise from a low-spin (ls) iron(I) center resulting from metal-based reduction, a ls-iron(II) (S = 0) center with a ligand-based radical, or an intermediate-spin (is) iron(II) (S = 1) center antiferromagnetically coupled to a ligand-based radical. An additional possibility is a high-spin (hs) iron(II) (S = 2) antiferromagnetically coupled to a ligand-based radical, but

this configuration would give rise to a total spin ground state of $S = 3/2$, which should exhibit g values spread over a much wider range than observed in Figure 11.[38] To make a definitive assignment, it is useful to draw comparisons with other mono-reduced BIP-iron complexes. For the mono-reduced complex $[(^{iPr}BIP)Fe(CO)_2](BAr^F_4)$, a rhombic EPR spectrum with $g = 2.111, 2.043, 1.994$ is observed and attributed to a low-spin Fe^I configuration with an $S = \frac{1}{2}$ ground state.[37] In contrast, the mono-reduced $[(^{iPr}BIP)Fe(OEt_2)](BAr^F_4)$ exhibits an EPR spectrum assigned to an $S = 3/2$ species derived from a high-spin Fe^{II} ion antiferromagnetically coupled to the BIP radical anion.[38] The spectrum in Figure 11 does not match the spectra for either of the former complexes. These results suggest that the LN_3S complex **4**, which contains a covalently tethered phenylthiolate group, exhibits a new electronic configuration consisting of either ls-Fe^{II} and a ligand-based radical or an is-Fe^{II} center antiferromagnetically coupled to a ligand-based radical, not previously observed in other mono-reduced complexes.

The in situ reduction of the nickel complex **5** helps clarify the EPR properties and electronic ground states of the LN_3S complexes described in this work. The mono-reduced analog of **5**, $[Ni(LN_3S)]^0$, was generated in situ and its EPR spectrum is shown in Figure 12. A sharp singlet at g 2.00 ($\Delta pp = 20$ G) is observed and can be assigned to a purely ligand-based radical.[70] Such a spectrum would be expected for **4** if this complex contained an ls-Fe^{II} ion and a single, unpaired e⁻ delocalized over the LN_3S ligand. Taken together, these data suggest that **4** may be best described as an intermediate-spin iron(II) ion antiferromagnetically coupled with a ligand radical, giving rise to the axial EPR spectrum in Figure 11.

Mössbauer Spectroscopy

Mössbauer spectra of microcrystalline samples of complexes **3** and **4** with natural abundance ^{57}Fe were collected at 5.3 K and with a weak applied field (47 mT) and are given in Figure 13. Mössbauer parameters for these complexes, together with complexes from the literature are given in Tables 4 and 5. Both **3** and **4** produced spectra that consisted of broad quadrupole doublets. The broad spectra may be attributed to the fact that the samples for **3** and **4** were mixtures of both crystalline and amorphous solids. The spectrum of **3** can be fitted to a quadrupole doublet with parameters that are highly distinctive[79] for a high-spin iron(II) ion ($\delta = 0.87$ mm s⁻¹; $\Delta E_Q = 2.70$ mm s⁻¹). However, the isomer shift is on the low end of the expected range, and this lowering is likely caused by both covalency of the thiolate iron bond and the five-coodinate nature of the complex. We previously reported an analogous ^{iPr}BIP complex, $[Fe^{II}(^{iPr}BIP)(SPh)Cl]$, which contains an exogenous thiolate donor in place of the tethered PhS⁻ group in **1 – 3** and Cl⁻ as the fifth ligand, and its Mössbauer spectrum was collected and is displayed in Figure S7.[25] Complex **3** and $[Fe^{II}(^{iPr}BIP)(SPh)Cl]$ exhibit similar isomer shifts and quadrupole splittings, suggesting that substitution of the neutral DMAP ligand with the anionic Cl⁻ ligand has little effect on the Mössbauer spectra and hence electronic structure. These complexes can also be compared favorably with data for the thiolate-ligated non-heme iron enzymes CDO[20] and SOR.[81]

We next examined the one-electron-reduced complex **4** by Mössbauer spectroscopy. Analysis of crystalline **4** affords a Mössbauer spectrum distinct from **3**, with a significant decrease in both isomer shift and quadrupole splitting ($\delta = 0.33$ mm s⁻¹; $\Delta E_Q = 2.04$ mm s⁻¹). Comparison with the mono- and doubly-reduced complexes in Table 5 show that **4** exhibits Mössbauer parameters in between those of mono-reduced $[(BIP)Fe(CO)_2]^+$, which contains two strong-field CO donors and an ls-Fe^I center, and mono-reduced $[(BIP)Fe(OEt_2)]^+$, which has a single, weak-field Et_2O donor and an hs-Fe^{II} ion. Surprisingly, the isomer shift and quadrupole splitting values for **4** are in fact closest to those seen for the *doubly-reduced* complexes, which have been assigned as intermediate-

spin (is) iron(II) species with diradical ligands. The Mössbauer data for **4** thus point to an is-Fe^{II} center as the best assignment for this complex, and this conclusion is in good agreement with both the structural and EPR data. The strong-field thiolate ligand in **4**, coupled with the relatively weak-field DMAP donor, gives rise to this unique electronic configuration.

Computational Studies

The iron(II) and nickel(II) complexes, and their mono-reduced analogs, were studied by DFT calculations to gain further insight into their structures and electronic configurations. The optimized geometries of [(LN$_3$S)Fe^{II}(DMAP)]$^+$ (**3**) and [Ni^{II}(LN$_3$S)]$^+$ (**5**) were calculated with the B3LYP functional on all low-lying spin states and are given in Figure 14. A quintet spin ground state ($S = 2$, hs-Fe^{II}) was found for **3**. At E+ZPE level of theory, the quintet state (^{5}**3**) for the iron(II) complex is more stable than either the triplet state ($S = 1$, is-Fe^{II}, (^{3}**3**)) or the singlet state (^{1}**3**) by 13.8 and 17.0 kcal mol^{-1}. Inclusion of dispersion corrections further increases the energy gaps to 21.6 and 32.7 kcal mol^{-1}, respectively. These results indicate that the singlet and triplet spin states should be inaccessible at room temperature, and match nicely with the experimental observations (structural parameters, ^{1}H NMR) that show **3** has an hs-Fe^{II} ground state. The Fe-N bond lengths in the DFT-optimized structure of ^{5}**3** range from 2.092 – 2.279 Å, and are in good agreement with the X-ray structure (Fe-N for **3**: 2.073(5) – 2.196(5)). The Fe-S distance of 2.407 Å for ^{5}**3** in Figure 14 is slightly elongated compared to the X-ray structure (Fe-S = 2.3246(18) Å). Note that when geometry optimizations for **3** were run with a pure density functional such as BP86 instead of B3LYP, a different spin state ordering was found, in which a degenerate singlet/triplet ground state was obtained and the quintet spin state was calculated to be much higher in energy (see Supporting Information). Consequently, pure density functional methods such as BP86 give results that are inconsistent with the experimental findings, and therefore we did not proceed further with these kinds of methods.

For the nickel(II) complex **5**, a closed-shell singlet spin state ($S = 0$) was found to be the ground state. We also calculated the triplet and quintet spin states for **5**, but found these states lie higher in energy than ^{1}**5** by 4.2 and 33.3 kcal mol^{-1}, respectively. No changes in spin state ordering were found for this complex when alternative density functional methods were employed. The optimized geometry for the ground state singlet is approximately square planar, consistent with the X-ray structure. The Ni-N distances for ^{1}**5** are in excellent agreement with those derived from the crystal structure (Table 3), although the Ni–S distance is slightly elongated (DFT: 2.201 Å; Expt: 2.1386(5) Å), similar to the trend seen for the Fe-S distance in ^{5}**3** versus the X-ray structure. The DFT calculations at the B3LYP level of theory often slightly overestimate metal-sulfur bond lengths.[83] The other main structural features, and importantly the spin ground states, are well reproduced by the calculations.

The mono-reduced complex **4** was also studied at the B3LYP level of theory, taking into consideration the possible doublet (S = ½) and quartet (S = 3/2) spin states for this complex. Calculations were initiated by using the coordinates from the X-ray structure of **4** as a starting point, and the results led to an overall doublet spin ground state ($S = \frac{1}{2}$) for the mono-reduced complex. The doublet spin state is found to be stabilized by 6.3 kcal mol^{-1} over the quartet spin state, and solvent corrections raise this energy gap to 6.5 kcal mol^{-1}, however dispersion corrections reduce it to 0.6 kcal mol^{-1}. The computationally-derived $S = 1/2$ ground state thus matches that derived from the EPR spectrum observed in Figure 9 for complex **4**. The bond distances for the doublet spin ground state of **4** are shown in Figure 14, and both the Fe-N and Fe-S distances are significantly shortened compared to the starting complex **3**. The Fe-N bond lengths for the in-plane LN$_3$S ligand are in good agreement with the structural parameters for **4** (Table 1), but the Fe-S distance is somewhat longer,

following the trend seen for **3** and **5**. In addition the Fe-N distance for the axial DMAP ligand is also slightly elongated (DFT: 2.170; Expt: 2.0508(16) Å).

The molecular orbital diagram for the doublet spin ground state of **4** is given in Figure 15 together with the MO diagram for the quintet spin ground state of starting complex **3**. For complex **4**, the computational results are consistent with an is-Fe^{II} ($S_{Fe} = 1$) center antiferromagnetically coupled with a ligand-based radical to give an overall doublet spin ($S_{total} = ½$) ground state. As seen in Figure 15, two α spin electrons reside in metal-based orbitals, while a predominantly ligand-based orbital (π^*_L) contains one β spin electron. The two unpaired electrons on the metal are reflected by a calculated spin density of $\rho_{Fe} = 1.96$, whereas the unpaired electron on the ligand leads to $\rho_{LN3S} = -1.00$ (Figure 14). In contrast, the MO diagram for **3** reveals four half-filled (α spin) metal-based orbitals resulting in $\rho_{Fe} = 3.74$, as expected for a hs-Fe^{II} center. The calculations show that one-electron reduction of **3** occurs by the filling of a low-lying virtual ligand (π^*_L) orbital in preference to filling of an empty metal-based orbital, confirming the non-innocent nature of the LN$_3$S ligand. The spin state change that occurs at the iron center upon reduction of **3** (hs-Fe^{II}) to **4** (is-Fe^{II}) appears to be a consequence of the destabilization of the σ^*_{xy} orbital. This destabilization is likely brought on by an increase in ligand field strength for the one-electron-reduced LN$_3$S ligand and a consequent shortening of the Fe-N and Fe-S bonds. Destabilization of σ^*_{xy} leads to depopulation of this orbital and occupation of the lower-lying π^*_{yz} orbital, resulting in an overall is-Fe^{II} center. Finally, the ligand-based β electron in **4** is mainly located on the bis(imino)pyridine backbone, which leads to the significant bond length perturbations shown in Figure 16, where the backbones for ^{5}**3** and ^{2}**4** are compared. The trends in the perturbations provide a satisfying match to what is seen experimentally in Figure 10 and help to further validate the DFT results. The close agreement of the calculated ligand backbone bond distances (Figure 16) with the X-ray structure of **4** provides additional evidence for the assignment of **4** as a one-electron reduced ligand radical coupled to an is-Fe^{II} ion ($\rho_{Fe} = 1.96$, $\rho_L = -1.00$; Figure 14a).

The mono-reduced product of ^{1}**5** was also investigated by DFT, giving the optimized geometry for the doublet spin ground state of ^{2}[Ni^{II}(LN$_3$S)]^0 shown in Figure 14. In this case, there are only very minor perturbations on the metal-ligand bond lengths as compared to the non-reduced starting material. Analysis of the spin density shows that the extra electron clearly lies on the LN$_3$S ligand and not the closed-shell nickel center, with an electron occupying a π^*_L orbital (Figure S8). The DFT calculations for the mono-reduced nickel complex provide further confirmation that LN$_3$S functions easily as a non-innocent ligand, and the ligand-based radical predicted by DFT is in full agreement with the sharp organic radical seen in the EPR spectrum for mono-reduced **5**.

O$_2$ Reactivity

We previously found that **1** reacts with excess O$_2$[24] in CH$_2$Cl$_2$ to give an S-oxygenated sulfonate complex, providing the first example of an Fe^{II}-thiolate complex that reacts with O$_2$ to give selective S-oxygenation. This reaction mimicked some of the general features of the reaction seen for CDO, but was lacking in the fact that the donor set at the metal center was N$_3$S(thiolate), not N$_4$S(thiolate), and the S-oxygenated product was a triply-oxygenated RSO$_3^-$ complex, as opposed to the doubly-oxygenated RSO$_2^-$ product generated by the enzymatic system. In a subsequent report, we prepared an improved N$_4$S(thiolate) iron(II) model complex based on the tripodal N4Py ligand, [Fe^{II}(N3PyS)(solvent)]$^+$, and found that it reacts with O$_2$ to give a biomimetic, doubly-oxygenated sulfinato-iron(II) complex.[26] We thus sought to test the new N$_4$S(thiolate) iron(II) complexes **2** and **3** to determine their reactivity toward O$_2$.

Reactions of complexes **2** and **3** with excess O_2 in CH_2Cl_2 were analyzed directly by LDIMS. The mass spectral data (Figures S3 and S4) show dominant ions that correspond to the triply-oxygenated sulfonato-iron(II) complex, $[Fe(LN_3SO_3)]^+$ ($m/z = 532$). This oxygenation pattern is the same as that seen for **1**. [24] Conversion of **1** to an N_4S(thiolate) coordination environment by addition of py or DMAP does not alter the O_2 reactivity such that S-oxygenation results in a doubly-oxygenated sulfinato product as seen for our other N_4S(thiolate) system.[25]

Some nickel(II) thiolate complexes can undergo S-oxygenation, most likely through a mechanism involving direct attack of O_2 on the coordinated sulfur atom, while other Ni^{II}-thiolates are inert toward O_2, and orbital compositions have been analyzed to explain these differences in O_2 reactivity.[46–54] We did not observe any reaction between complex **5** and excess O_2 in CH_2Cl_2, even after prolonged stirring for several days. Solutions of the mono-reduced nickel(II) complex $[Ni(LN_3S)]^0$ generated from Na/Hg amalgam in THF were next tested for their reactivity toward O_2. In this case a rapid reaction with O_2 was indeed observed by an immediate color change from bright to dark green, but LDI-MS analysis of the reaction mixture revealed only a peak ($m/z = 488.3$, Figure S6) for the starting material **5**, suggesting only outer-sphere oxidation had occurred. In contrast, a related $Ni^{II}(BIP)$ complex undergoes outer-sphere reduction to give a one-electron reduced product that then reacts with O_2 via an inner-sphere mechanism to afford ligand-oxidized products.[70]

The mono-reduced compound **4** also exhibits rapid reactivity with O_2. Exposure of solutions of **4** in Et_2O to air, or bubbling O_2, leads to an immediate color change from dark green to brown with concurrent formation of a brown precipitate. Analysis by LDI-MS reveals a mixture that can be assigned to Fe-oxygenates and S-oxygenates, with multiple major peaks assigned to $[SOFe^{III}-O-Fe^{III}SO]^{2+}$ ($m/z = 508.3$), $[SO_2Fe^{III}-O-Fe^{III}SO_2]^{2+}$ ($m/z = 524.4$), and $[SO_3Fe^{III}-O-Fe^{III}-SO_3]^{2+}$ ($m/z = 540.4$), see Figure S5. While complexes **1 – 3** exhibit S-centered oxidation, the mono-reduced complex **4** appears to show significant oxidation at the iron center. This represents a significant change in the observed reactivity of these complexes as a result of the change in electronic structure.

Conclusions

The triflate-ligated ferrous complex $[Fe^{II}(LN_3S)OTf]$ (**1**) serves as a useful precursor for the facile synthesis of the biomimetic N_4S(thiolate) complexes $[Fe^{II}(LN_3S)(DMAP)]OTf$ (**2**) and $[Fe^{II}(LN_3S)(DMAP)]OTf$ (**3**). Template assembly with nickel(II) tetrafluoroborate leads to the Ni^{II} analog $[Ni^{II}(LN_3S)]BF_4$ (**5**). Structural and spectroscopic methods show that the iron complexes are 5-coordinate, high-spin ($S = 2$) iron(II) species, while the nickel complex is a 4-coordinate square-planar nickel(II) species. Electrochemical measurements revealed that these complexes uniformly exhibit only one reversible reduction wave between −0.9 and −1.2 V vs Fc^+/Fc within the CH_3CN solvent window. Bulk chemical reduction of **3** by Na/Hg amalgam gives the extremely air-sensitive, mono-reduced complex $[Fe(LN_3S)(DMAP)]^0$ (**4**), which was isolated and crystallographically characterized. No evidence for a two-electron reduced product was observed, in line with the electrochemical analysis. This behavior contrasts other bis(imino)pyridine complexes, which typically can house up to two or three reducing equivalents beginning at the $M^{2+}(BIP^0)$ redox level, and have been shown to form two-electron reduced products from Na/Hg reduction. It can be concluded that the anionic thiolate arm appended to the new LN_3S system likely causes multiple reductions to be thermodynamically unfavorable. The X-ray structure of **4** shows it is a 5-coordinate complex, with one DMAP ligand remaining coordinated in the axial position following reduction. The electronic structure of the mono-reduced complex **4** was firmly established through a combination of structural analysis, EPR and Mössbauer spectroscopies as well as computational (DFT) methods. The ground state of **4** is clearly a doublet state that arises

from an intermediate-spin ($S = 1$) iron(II) center antiferromagnetically coupled to a ligand-based radical. The spin state of the iron center is reflected in the unusual Mössbauer parameters for this mono-reduced BIP complex, with $ = 0.33$ mm s^{-1} and E$_q = 2.04$ mm s^{-1}. These parameters differ significantly from other mono-reduced Fe(BIP) complexes that exhibit either hs-Fe^{II} ($S = 2$) or ls-Fe^{II} ($S = 0$) configurations, and in fact fall in line with the doubly-reduced Fe(BIP) species which have been previously assigned as is-Fe^{II} complexes carrying diradical ligands. The computational studies show that the doublet spin ground state is comprised of two   electrons occupying metal-based orbitals of d_{z2} and d_{xz} parentage and one   electron residing on a ligand-based   * orbital with most of the spin density localized on the bis(imino)pyridine backbone and not on the phenylthiolate arm. The DFT results are nicely validated by their agreement with the findings from Mössbauer and EPR spectroscopies, as well as by their reproduction of the experimentally observed, yet subtle bond length distortions that occur in the BIP backbone upon one-electron reduction. This study shows that the tetradentate LN$_3$S ligand can serve as a non-innocent ligand in the same fashion as the parent BIP system, but in this case only accepts one electron delocalized over the ligand backbone. Taken together, our experimental and computational data strongly suggest that mono-reduction of the starting iron(II) complex provides the first example of an intermediate-spin iron(II) complex antiferromagnetically coupled with a ligand-based radical.

The O$_2$ reactivity of the new Fe^{II} complexes **2** and **3** appears to mirror that of **1** to give sulfonato-iron complexes. Interestingly, the thiolate-ligated Ni^{II} complex **5** is completely unreactive toward O$_2$, as opposed to some thiolate-ligated Ni^{II} complexes that can become oxygenated at the sulfur positions. The mono-reduced iron complex **4** is extremely air-sensitive and rapidly reacts with O$_2$, but instead of leading only to S-oxygenation, yields a mixture of products involving both Fe-centered and S-centered oxygenates. Now that the ability to store reducing equivalents on thiolate-appended BIP ligands has been established, future work may involve designing systems where reducing equivalents on both the non-innocent ligand and the metal can be harnessed in a more controlled fashion for O$_2$ activation.

Supplementary Material

Refer to Web version on PubMed Central for supplementary material.

Acknowledgments

References

1. McQuilken AC, Goldberg DP. Dalton Trans. 2012; 41:10883. [PubMed: 22814765]

2. Fox, BG. Iron cofactors: Non-heme Handbook of Proteins. John Wiley&Sons Ltd; Chichester, UK: 2007. p. 611-618.

3. Kovacs JA, Brines LM. Acc Chem Res. 2007; 40:501. [PubMed: 17536780]

4. Mascharak PK. Coord Chem Rev. 2002; 225:201.

5. Solomon EI, Decker A, Lehnert N. Proc Natl Acad Sci U S A. 2003; 100:3589. [PubMed: 12598659]

6. Ryle MJ, Hausinger RP. Curr Opin Chem Biol. 2002; 6:193. [PubMed: 12039004]

7. Bruijnincx PCA, van Koten G, Gebbink RJMK. Chem Soc Rev. 2008; 37:2716. [PubMed: 19020684]

8. Nivière V, Bonnot F, Bourgeois D. Handb Metalloproteins. 2011:246.

9. Yeh AP, Hu YL, Jenney FE, Adams MWW, Rees DC. Biochemistry. 2000; 39:2499. [PubMed: 10704199]

10. Matias PM, Morais J, Coelho AV, Meijers R, Gonzalez A, Thompson AW, Sieker L, LeGall J, Carrondo MA. J Biol Inorg Chem. 1997; 2:507.

11. Santos-Silva T, Trincão J, Carvalho AL, Bonifàcio C, Auchère F, Raleiras P, Moura I, Moura JJG, Romão MJ. J Biol Inorg Chem. 2006; 11:548. [PubMed: 16791639]

12. Adam V, Royant A, Niviere V, Molina-Heredia FP, Bourgeois D. Structure. 2004; 12:1729. [PubMed: 15341736]

13. Kobayashi M, Nagasawa T, Yamada H. Trends Biotechnol. 1992; 10:402. [PubMed: 1368882]

14. Endo I, Nojiri M, Tsujimura M, Nakasako M, Nagashima S, Yohda M, Odaka M. J Inorg Biochem. 2001; 83:247. [PubMed: 11293544]

15. Kobayashi M, Shimizu S. Nat Biotechnol. 1998; 16:733. [PubMed: 9702770]

16. de Visser, SP.; Kumar, D., editors. Iron-Containing Enzymes: Versatile Catalysts of Hydroxylation Reactions in Nature. Royal Society of Chemistry; Cambridge, U.K: 2011.

17. Joseph CA, Maroney MJ. Chem Commun. 2007:3338.

18. Straganz GD, Nidetzky B. Chembiochem. 2006; 7:1536. [PubMed: 16858718]

19. Siakkou E, Rutledge MT, Wilbanks SM, Jameson GNL. Biochim Biophys Acta, Proteins Proteomics. 2011; 1814:2003.

20. Tchesnokov EP, Wilbanks SM, Jameson GNL. Biochemistry. 2012; 51:257. [PubMed: 22122511]

21. McCoy JG, Bailey LJ, Bitto E, Bingman CA, Aceti DJ, Fox BG, Phillips GN. Proc Natl Acad Sci U S A. 2006; 103:3084. [PubMed: 16492780]

22. Simmons CR, Liu Q, Huang QQ, Hao Q, Begley TP, Karplus PA, Stipanuk MH. J Biol Chem. 2006; 281:18723. [PubMed: 16611640]

23. Ye S, Wu X, Wei L, Tang DM, Sun P, Bartlam M, Rao ZH. J Biol Chem. 2007; 282:3391. [PubMed: 17135237]

24. Jiang YB, Widger LR, Kasper GD, Siegler MA, Goldberg DP. J Am Chem Soc. 2010; 132:12214. [PubMed: 20712312]

25. Badiei YM, Siegler MA, Goldberg DP. J Am Chem Soc. 2011; 133:1274. [PubMed: 21207980]

26. McQuilken AC, Jiang YB, Siegler MA, Goldberg DP. J Am Chem Soc. 2012; 134:8758. [PubMed: 22578255]

27. Kovacs JA. Science. 2003; 299:1024. [PubMed: 12586930]

28. Kovacs JA. Chem Rev. 2004; 104:825. [PubMed: 14871143]

29. Artaud I, Chatel S, Chauvin AS, Bonnet D, Kopf MA, Leduc P. Coord Chem Rev. 1999; 192:577.

30. Cho J, Woo J, Nam W. J Am Chem Soc. 2012; 134:11112. [PubMed: 22713134]

31. Sallmann M, Siewert I, Fohlmeister L, Limberg C, Knispel C. Angew Chem Int Ed. 2012; 51:2234.

32. Gonzalez-Ovalle LE, Quesne MG, Kumar D, Goldberg DP, de Visser SP. Org Biomol Chem. 2012; 10:5401. [PubMed: 22714822]

33. Kumar D, Sastry GN, Goldberg DP, de Visser SP. J Phys Chem A. 2012; 116:582. [PubMed: 22091701]

34. Britovsek GJP, Bruce M, Gibson VC, Kimberley BS, Maddox PJ, Mastroianni S, McTavish SJ, Redshaw C, Solan GA, Stromberg S, White AJP, Williams DJ. J Am Chem Soc. 1999; 121:8728.

35. Scott J, Gambarotta S, Korobkov I, Budzelaar PHM. Organometallics. 2005; 24:6298.

36. Scott J, Gambarotta S, Korobkov I, Knijnenburg Q, de Bruin B, Budzelaar PHM. J Am Chem Soc. 2005; 127:17204. [PubMed: 16332066]

37. Tondreau AM, Milsmann C, Lobkovsky E, Chirik PJ. Inorg Chem. 2011; 50:9888. [PubMed: 21667935]

38. Tondreau AM, Stieber SCE, Milsmann C, Lobkovsky E, Weyhermuller T, Semproni SP, Chirik PJ. Inorg Chem. 2013; 52:635. [PubMed: 23268722]

39. Bart SC, Chlopek K, Bill E, Bouwkamp MW, Lobkovsky E, Neese F, Wieghardt K, Chirik PJ. J Am Chem Soc. 2006; 128:13901. [PubMed: 17044718]

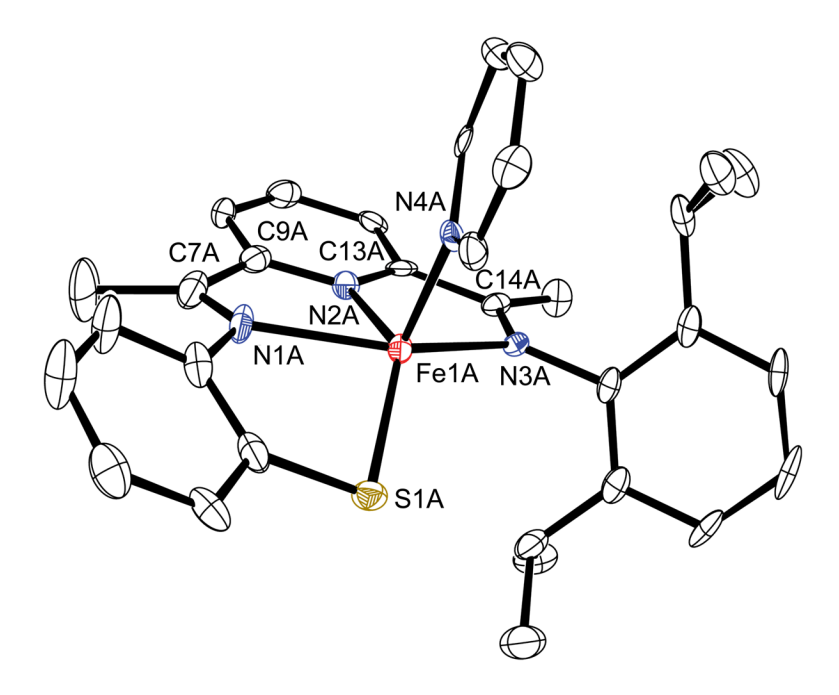40. Bouwkamp MW, Bart SC, Hawrelak EJ, Trovitch RJ, Lobkovsky E, Chirik PJ. Chem Commun. 2005:3406.

41. Bart SC, Lobkovsky E, Bill E, Wieghardt K, Chirik PJ. Inorg Chem. 2007; 46:7055. [PubMed: 17655227]

42. Stieber SCE, Milsmann C, Hoyt JM, Turner ZR, Finkelstein KD, Wieghardt K, DeBeer S, Chirik PJ. Inorg Chem. 2012; 51:3770. [PubMed: 22394054]

43. Darmon JM, Turner ZR, Lobkovsky E, Chirik PJ. Organometallics. 2012; 31:2275. [PubMed: 22675236]

44. Enright D, Gambarotta S, Yap GPA, Budzelaar PHM. Angew Chem Int Ed. 2002; 41:3873.

45. de Bruin B, Bill E, Bothe E, Weyhermuller T, Wieghardt K. Inorg Chem. 2000; 39:2936. [PubMed: 11232835]

46. Farmer PJ, Solouki T, Mills DK, Soma T, Russell DH, Reibenspies JH, Darensbourg MY. J Am Chem Soc. 1992; 114:4601.

47. Farmer PJ, Solouki T, Soma T, Russell DH, Darensbourg MY. Inorg Chem. 1993; 32:4171.

48. Darensbourg MY, Tuntulani T, Reibenspies JH. Inorg Chem. 1995; 34:6287.

49. Buonomo RM, Font I, Maguire MJ, Reibenspies JH, Tuntulani T, Darensbourg MY. J Am Chem Soc. 1995; 117:5427.

50. Grapperhaus CA, Darensbourg MY, Sumner LW, Russell DH. J Am Chem Soc. 1996; 118:1791.

51. Grapperhaus CA, Darensbourg MY. Acc Chem Res. 1998; 31:451.

52. Mullins CS, Grapperhaus CA, Frye BC, Wood LH, Hay AJ, Buchanan RM, Mashuta MS. Inorg Chem. 2009; 48:9974. [PubMed: 19795870]

53. Herdt DR, Grapperhaus CA. Dalton Trans. 2012; 41:364. [PubMed: 22105369]

54. Mullins CS, Grapperhaus CA, Kozlowski PM. J Biol Inorg Chem. 2006; 11:617. [PubMed: 16724228]

55. Kumar D, Karamzadeh B, Sastry GN, de Visser SP. J Am Chem Soc. 2010; 132:7656. [PubMed: 20481499]

56. Vardhaman AK, Sastri CV, Kumar D, de Visser SP. Chem Commun. 2011; 47:11044.

57. Becke AD. J Chem Phys. 1993; 98:1372.

58. Lee CT, Yang WT, Parr RG. Phys Rev B. 1988; 37:785.

59. Hay PJ, Wadt WR. J Chem Phys. 1985; 82:299.

60. Grimme S, Antony J, Ehrlich S, Krieg H. J Chem Phys. 2010; 132:154104. [PubMed: 20423165]

61. Becke AD. Phys Rev A. 1988; 38:3098. [PubMed: 9900728]

62. Perdew JP. Phys Rev B. 1986; 33:8822.

63. Jaguar, version 7.9. Schrödinger, LLC; New York, NY: 2011.

64. Schwabe T, Grimme S. Phys Chem Chem Phys. 2007; 9:3397. [PubMed: 17664963]

65. Bianchini C, Mantovani G, Meli A, Migliacci F, Zanobini F, Laschi F, Sommazzi A. Eur J Inorg Chem. 2003:1620.

66. Fiedler AT, Halfen HL, Halfen JA, Brunold TC. J Am Chem Soc. 2005; 127:1675. [PubMed: 15701002]

67. Theisen RM, Shearer J, Kaminsky W, Kovacs JA. Inorg Chem. 2004; 43:7682. [PubMed: 15554633]

68. Shearer J, Nehring J, Lovell S, Kaminsky W, Kovacs JA. Inorg Chem. 2001; 40:5483. [PubMed: 11599942]

69. Addison AW, Rao TN, Reedijk J, Vanrijn J, Verschoor GC. J Chem Soc, Dalton Trans. 1984:1349.

70. Manuel TD, Rohde JU. J Am Chem Soc. 2009; 131:15582. [PubMed: 19860475]

71. Fan RQ, Fan RJ, Lv ZW, Yang YL, An F, Gu DM. J Coord Chem. 2007; 60:919.

72. Dunn TJ, Ramogida CF, Simmonds C, Paterson A, Wong EWY, Chiang L, Shimazaki Y, Storr T. Inorg Chem. 2011; 50:6746. [PubMed: 21675708]

73. Chen YJ, Hao P, Zuo WW, Gao K, Sun WH. J Organomet Chem. 2008; 693:1829.

74. Bryliakov KP, Talsi EP, Semikolenova NV, Zakharov VA. Organometallics. 2009; 28:3225.

75. Britovsek GJP, Gibson VC, Spitzmesser SK, Tellmann KP, White AJP, Williams DJ. J Chem Soc, Dalton Trans. 2002:1159.

76. Bart SC, Lobkovsky E, Chirik PJ. J Am Chem Soc. 2004; 126:13794. [PubMed: 15493939]

77. Nakajima Y, Nakao Y, Sakaki S, Tamada Y, Ono T, Ozawa F. J Am Chem Soc. 2010; 132:9934. [PubMed: 20593821]

78. Trovitch RJ, Lobkovsky E, Chirik PJ. J Am Chem Soc. 2008; 130:11631. [PubMed: 18686955]

79. Gütlich, P.; Bill, E.; Trautwein, AX. Mössbauer Spectroscopy and Transition Metal Chemistry: Fundamentals and Applications. Springer-Verlag; Berlin Heidelberg: 2011.

80. Britovsek GJP, Clentsmith GKB, Gibson VC, Goodgame DML, McTavish SJ, Pankhurst QA. Catal Commun. 2002; 3:207.

81. Moura I, Tavares P, Moura JJG, Ravi N, Huynh BH, Liu MY, Legall J. J Biol Chem. 1990; 265:21596. [PubMed: 2174880]

82. Russell SK, Milsmann C, Lobkovsky E, Weyhermuller T, Chirik PJ. Inorg Chem. 2011; 50:3159. [PubMed: 21395246]

83. Kumar D, Thiel W, de Visser SP. J Am Chem Soc. 2011; 133:3869. [PubMed: 21344861]

Figure 1.
Complexes described in the present study.

Figure 2.
Displacement ellipsoid plot for the cation of complex **2** (50% probablility level). The H atoms are removed for clarity.
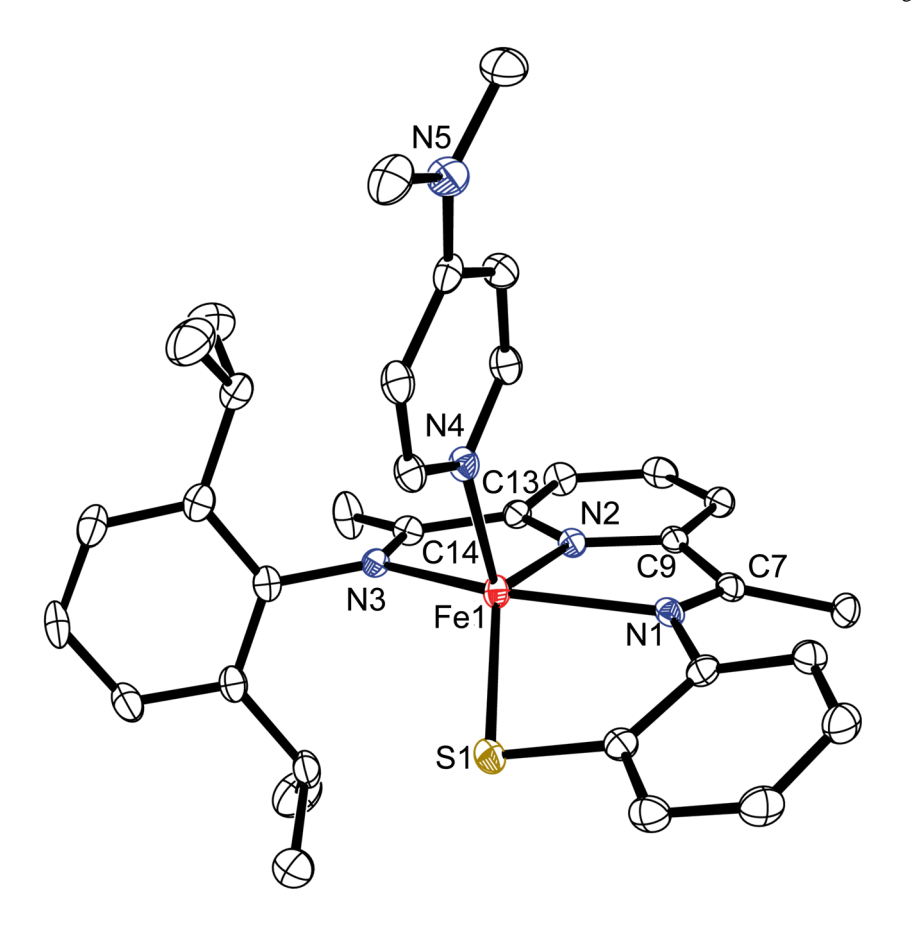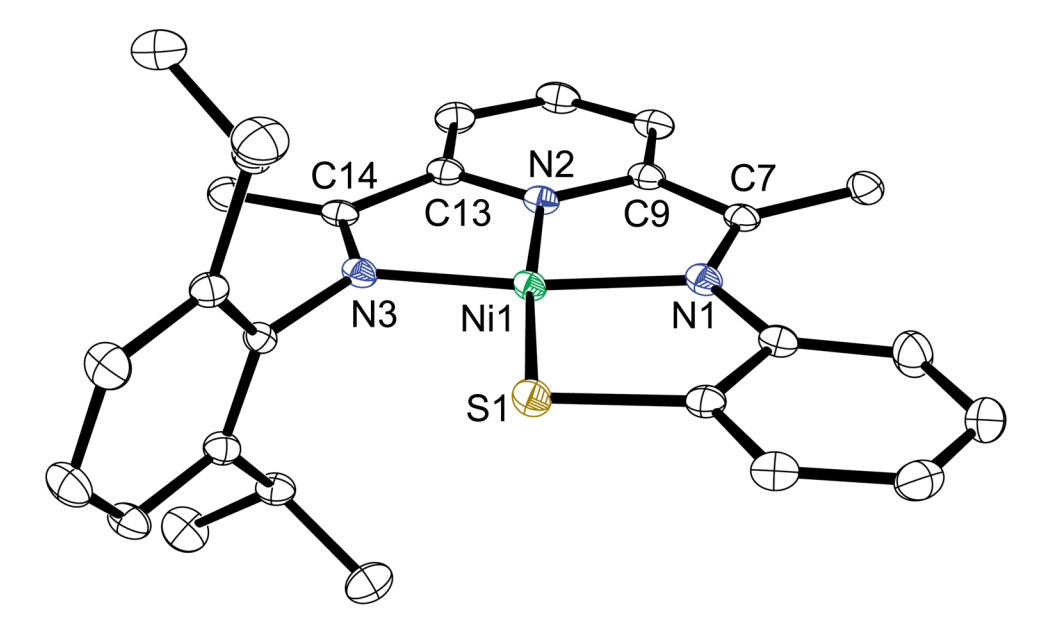
Figure 3.
Displacement ellipsoid plot for the cation of complex **3** (50% probablility level). The H atoms are removed for clarity.
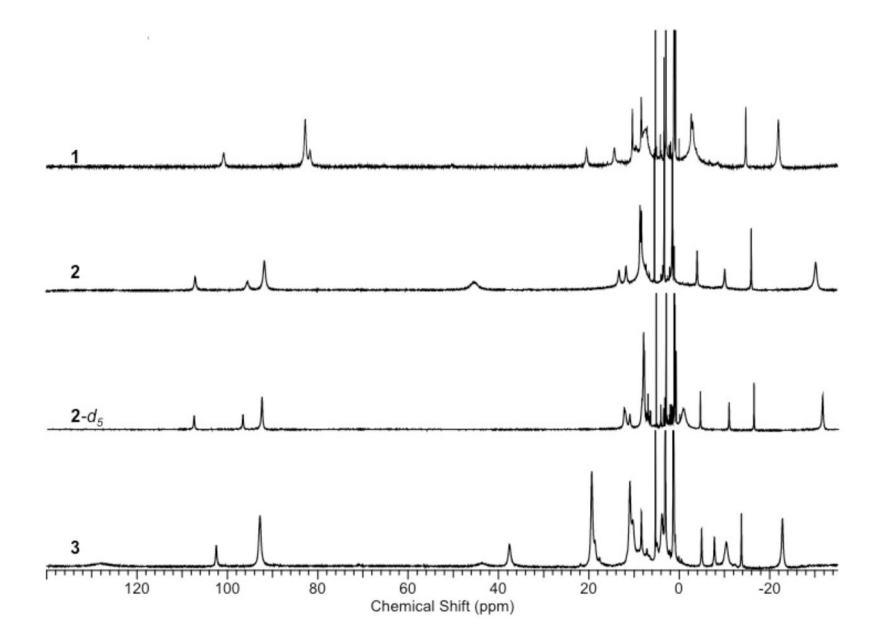
Figure 4.
Displacement ellipsoid plot for the cation of complex **5** (50% probablility level). The H atoms are removed for clarity.

Figure 5.
^{1}H-NMR spectra of complexes **1 – 3** in CD_2Cl_2 at 25 °C.
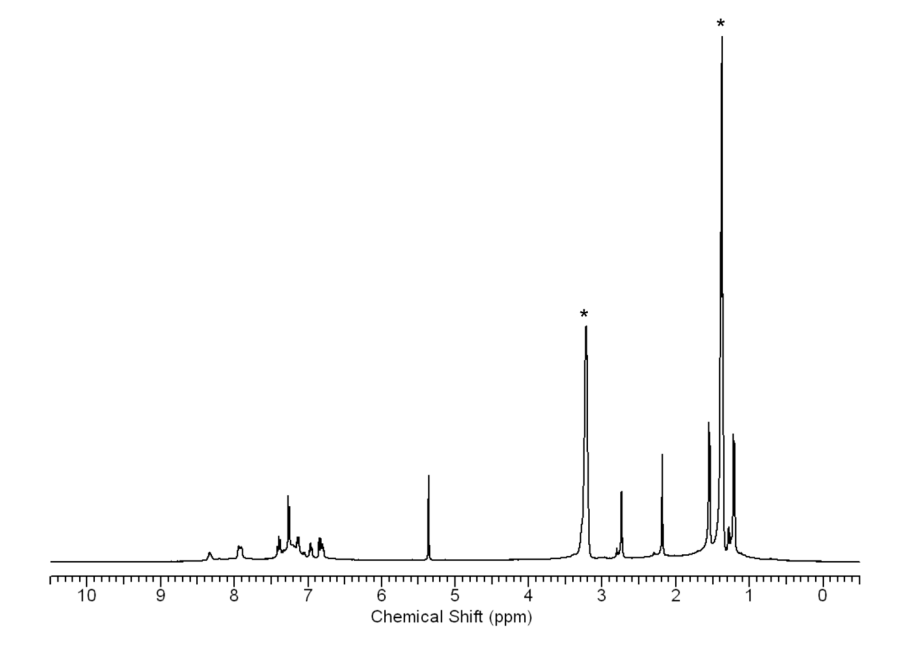
Figure 6.
^{1}H NMR spectrum of **5** in CD_2Cl_2 at 25 °C. $Et_3NH^+BF_4^-$ impurity (*).
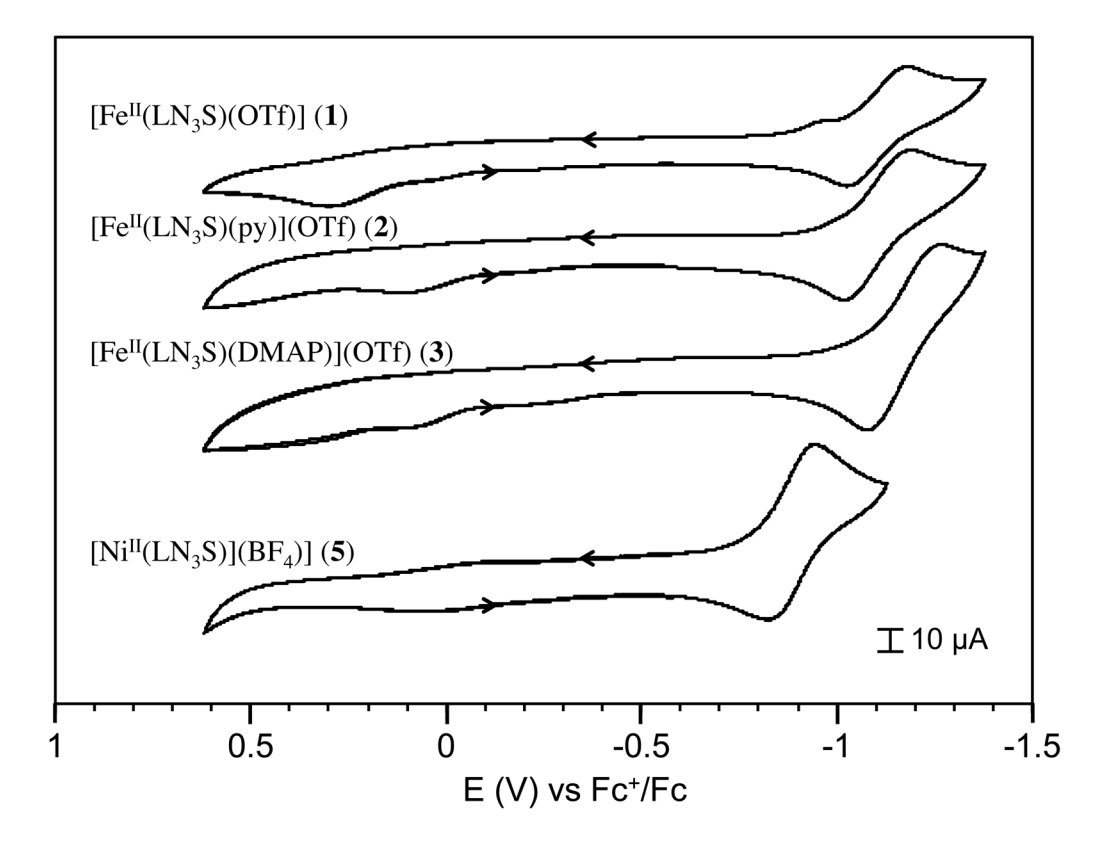
Figure 7.
Cyclic voltammograms of compounds **1** – **3** and **5** in MeCN. $E_{1/2}$: (**1**) = −1.1 V, (**2**) = −1.1 V, (**3**) = −1.2 V, (**5**) = −0.9 V; E_p: (**1**) = 120 mV, (**2**) = 130 mV, (**3**) = 130 mV, (**5**) = 66 mV. Working electrode: glassy carbon; counter electrode: platinum; reference electrode: Ag/Ag$^+$. Electrolyte: LiClO$_4$, 100 mM. Scan rate: 100 mV/s.
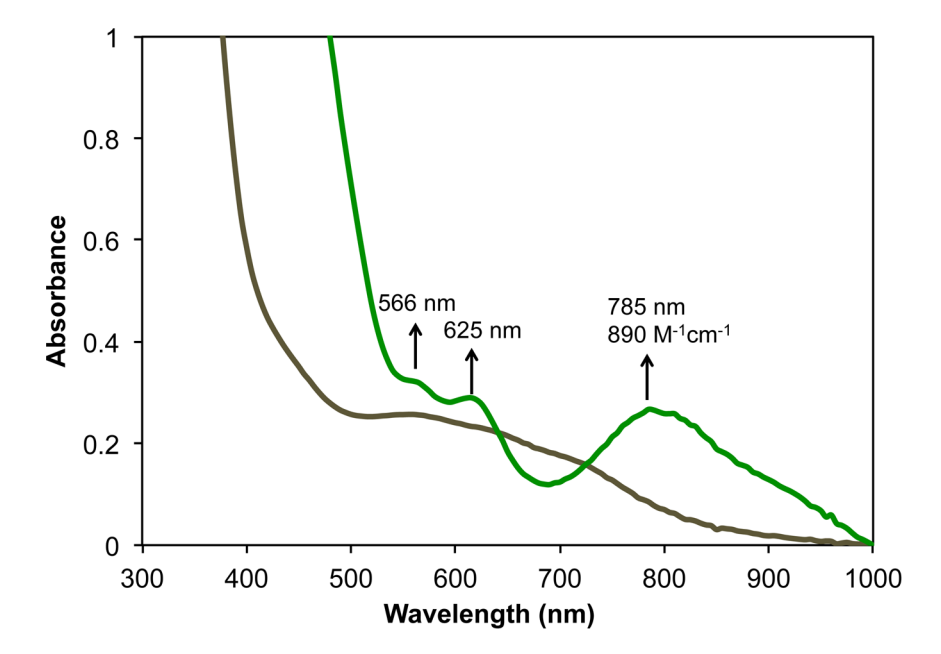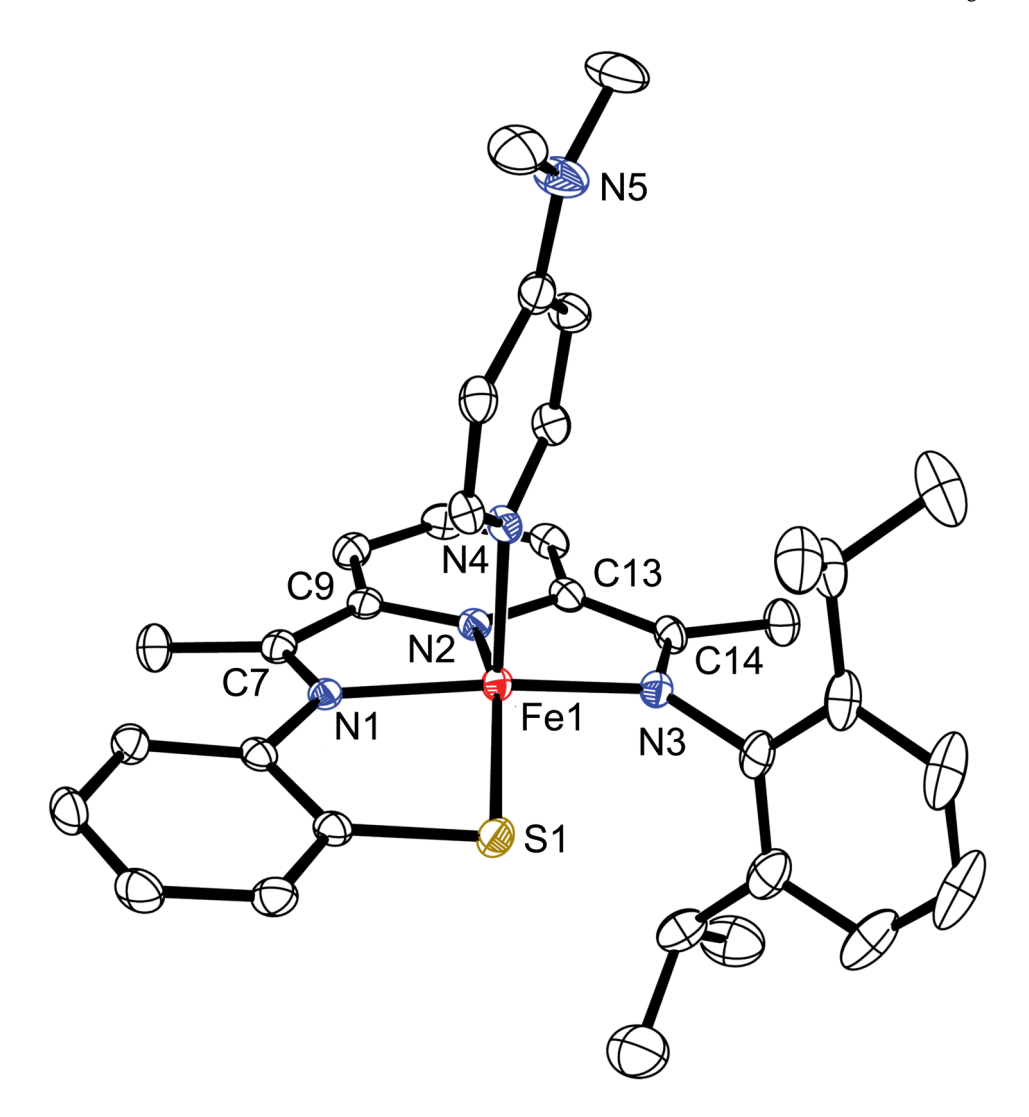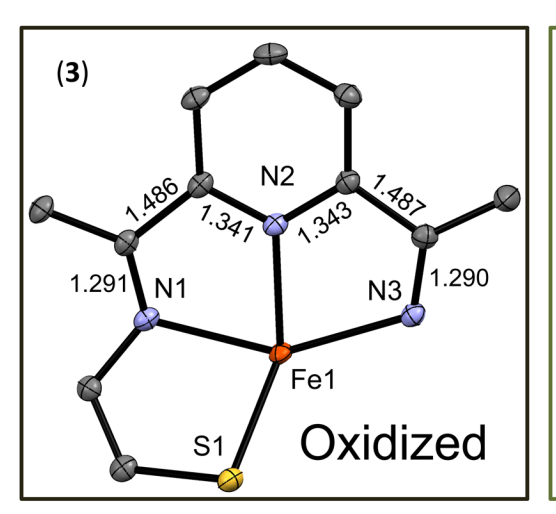
Figure 8.
UV-vis spectral change for the conversion of **3** (brown) to **4** (green) with 0.5% Na/Hg amalgam in THF.

Figure 9.
Displacement ellipsoid plot for **4** (50% probablility level). The H atoms are removed for clarity.
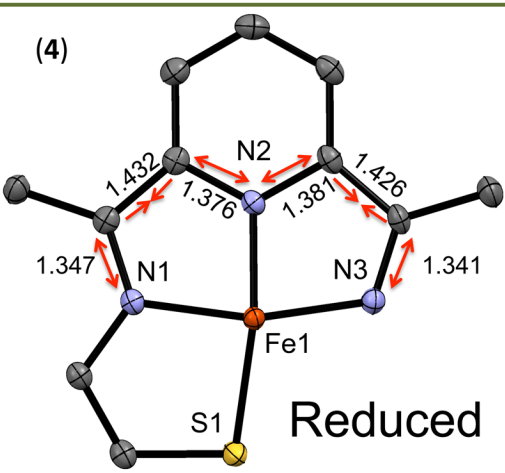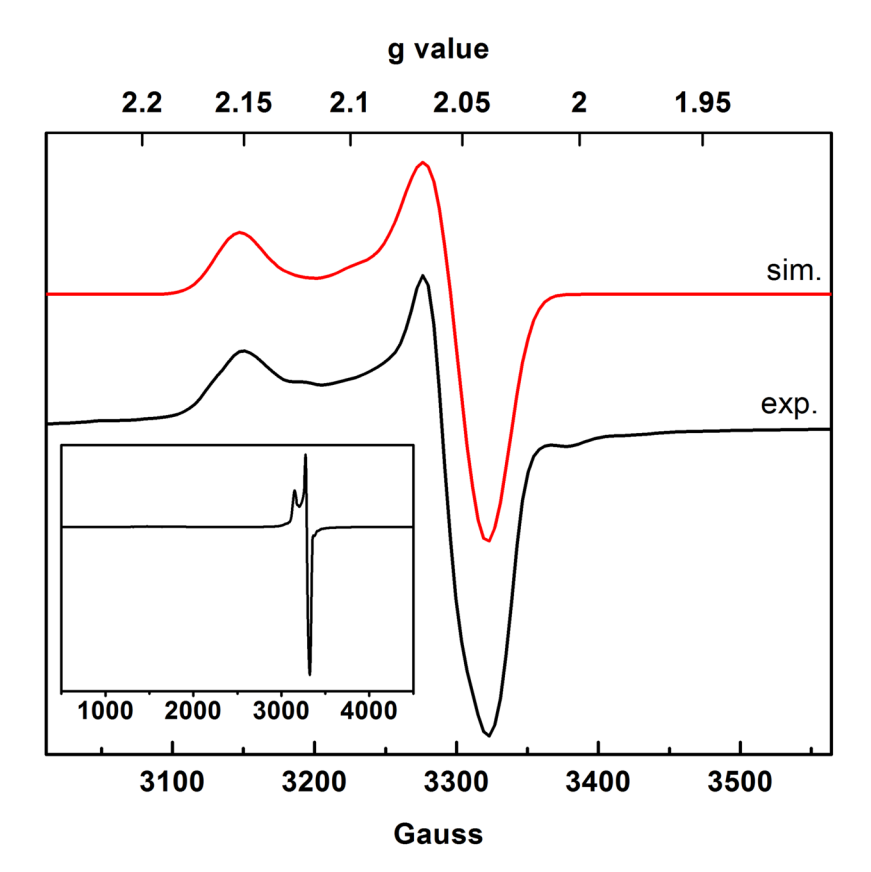
Figure 10.
Comparison of selected ligand bond lengths for **3** (left) and **4** (right).

Figure 11.
X-band EPR spectrum of **4** (2.4 mM) in Et_2O at 16 K (black line). Inset: full-range experimental spectrum. Parameters: frequency, 9.479 GHz; microwave power, 2 mW; modulation amplitude, 10 G; modulation frequency, 100 kHz. Parameters for simulation (red line): $S = ½$; g = [2.155, 2.057, 2.038]; Lorentzian linewidths, W = 33, 32, and 30 G.

Figure 12.
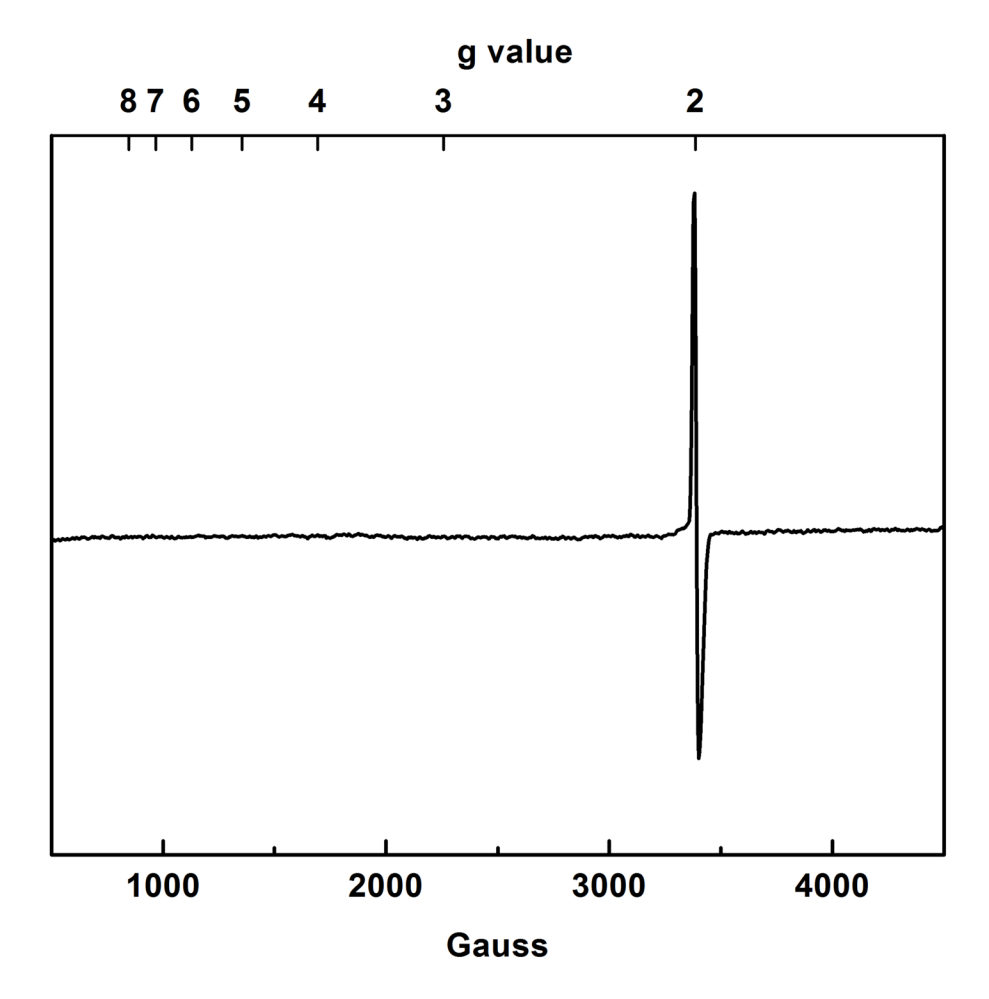X-band EPR spectrum of **5** (3.0 mM) + Na/Hg (0.5%) amalgam in THF at 16 K. Parameters: frequency, 9.479 GHz; microwave power, 2 mW; modulation amplitude, 10 G; modulation frequency, 100 kHz.
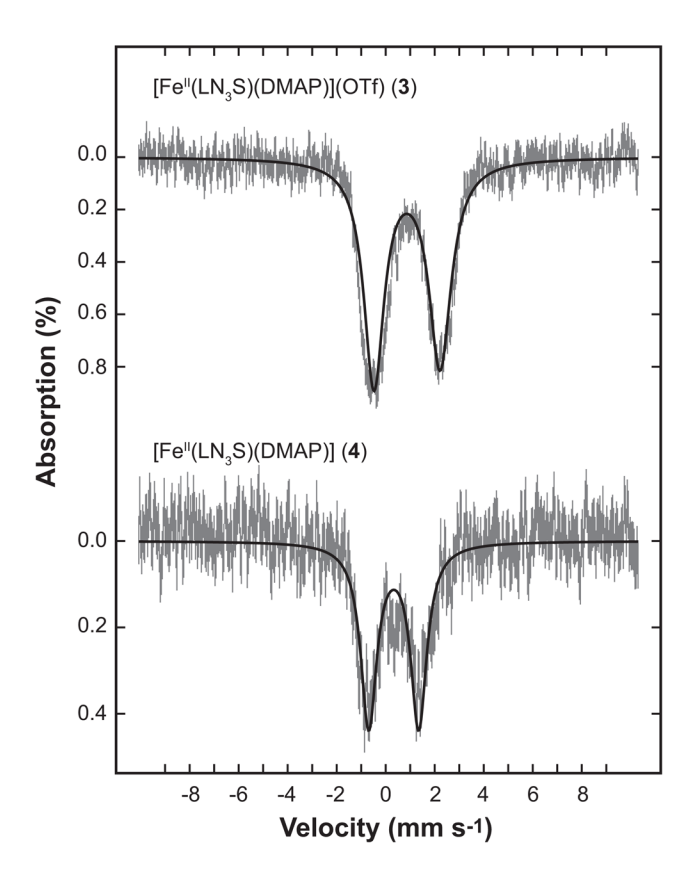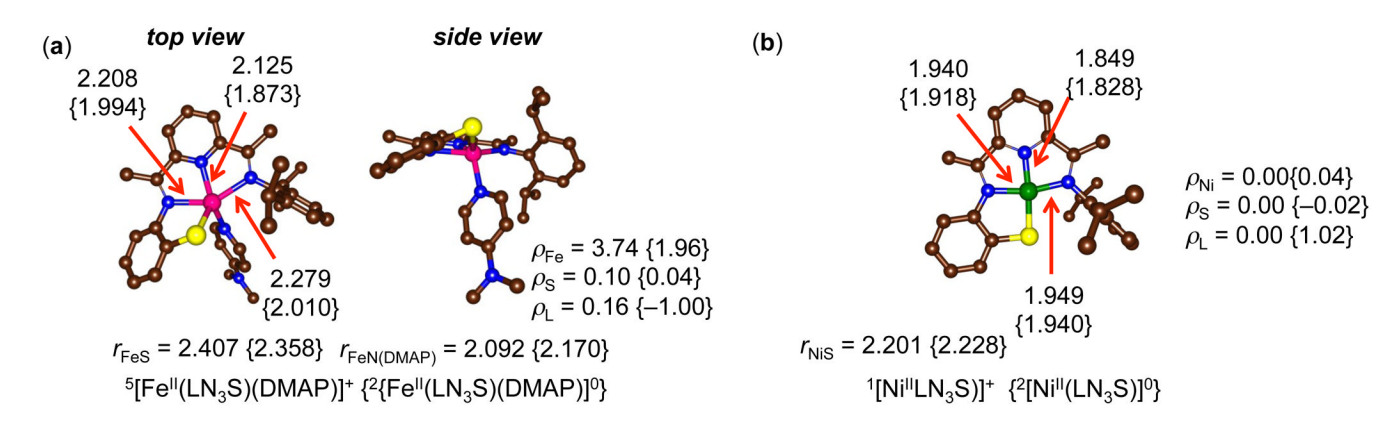
Figure 13.
Mössbauer spectra at 5.3 K in a weak applied field (47 mT) of **3** (starting material) and **4** (mono-reduced). Both spectra consist of broad quadrupole doublets ($\Gamma_{L=R} = 0.8$ mm s^{-1}). Complex **3** has parameters that can be assigned to a high-spin iron(II) species: ($\delta = 0.87$ mm s^{-1}; $\Delta E_Q = 2.70$ mm s^{-1}), while **4** is consistent with an intermediate-spin iron(II) species coupled to a S=½ radical: ($\delta = 0.33$ mm s^{-1}; $\Delta E_Q = 2.04$ mm s^{-1}).

(a) *top view* *side view*

2.208 {1.994}   2.125 {1.873}

2.279 {2.010}

ρ_{Fe} = 3.74 {1.96}
ρ_S = 0.10 {0.04}
ρ_L = 0.16 {−1.00}

r_{FeS} = 2.407 {2.358} $r_{FeN(DMAP)}$ = 2.092 {2.170}

$^5[Fe^{II}(LN_3S)(DMAP)]^+$ $\{^2\{Fe^{II}(LN_3S)(DMAP)]^0\}$

(b) 1.940 {1.918}   1.849 {1.828}

ρ_{Ni} = 0.00{0.04}
ρ_S = 0.00 {−0.02}
ρ_L = 0.00 {1.02}

1.949 {1.940}

r_{NiS} = 2.201 {2.228}

$^1[Ni^{II}LN_3S)]^+$ $\{^2[Ni^{II}(LN_3S)]^0\}$

Figure 14.
Optimized UB3LYP/B1 geometries of $^5[Fe^{II}(LN_3S)(DMAP)]^+$ and $^1[Ni^{II}(LN_3S)]^+$, and their reduced complexes with bond lengths in angstroms. Also given are group spin densities.
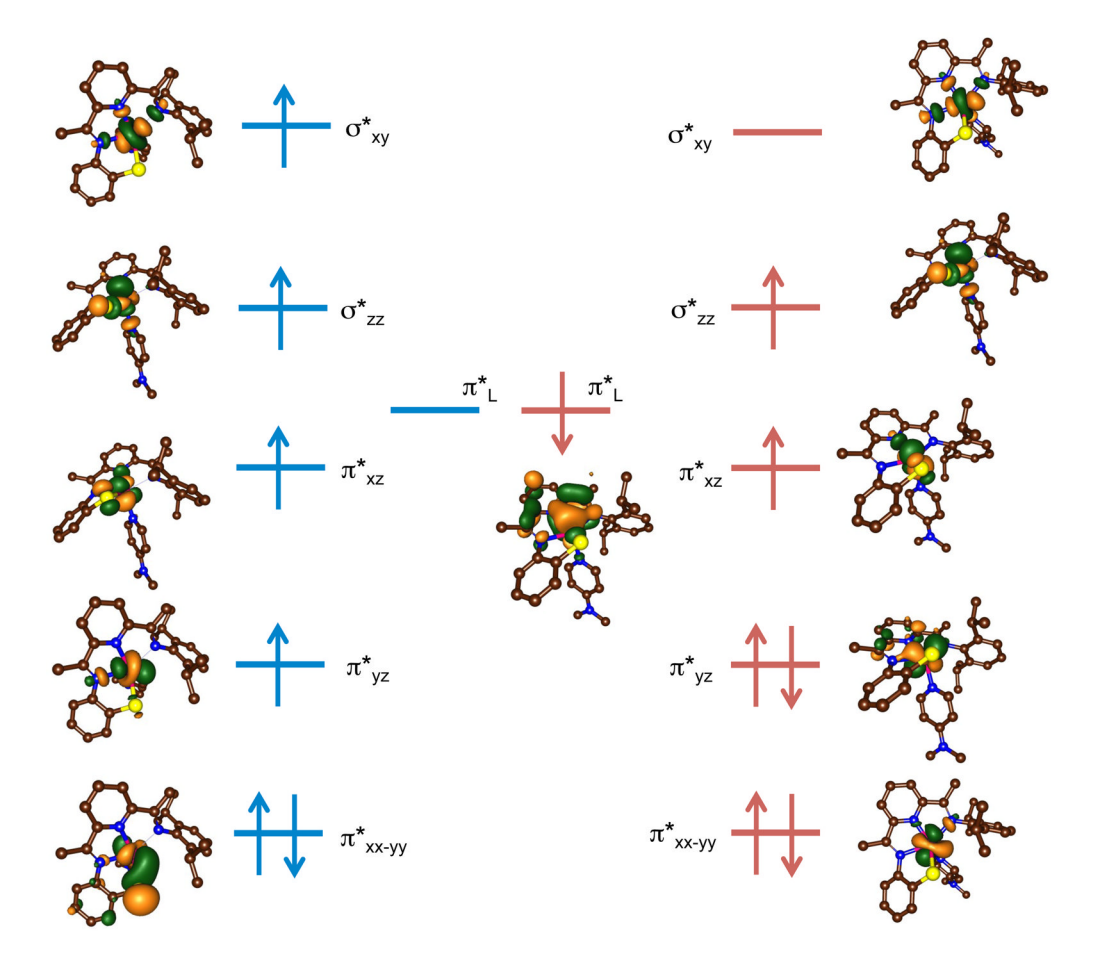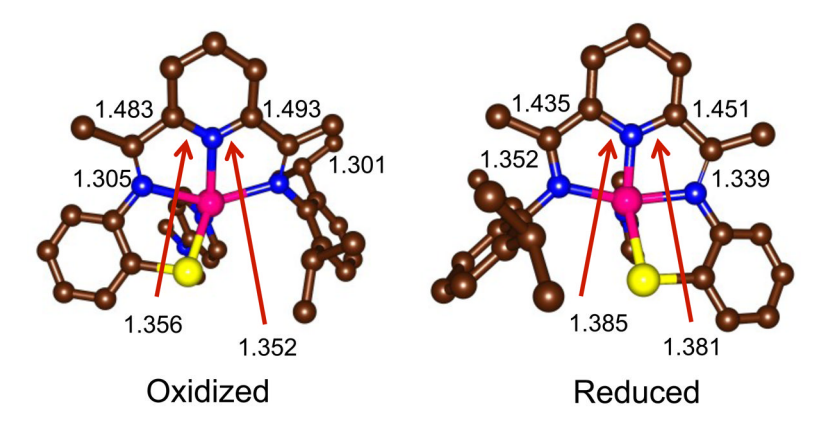
Figure 15.
Orbital diagrams of $^5[Fe^{II}(LN_3S)(DMAP)]^+$ (left) and $^2[Fe^{II}(LN_3S)(DMAP)]^0$ (right).

Figure 16.
Optimized UB3LYP/B1 geometries of $^5[Fe^{II}(LN_3S)(DMAP)]^+$ and $^2[Fe^{II}(LN_3S)(DMAP)]^0$, highlighting BIP ligand backbone bond lengths in angstroms.

Scheme 1.
Synthesis of Iron(II) Complexes (1 – 3), and Nickel(II) Complex (5)

Scheme 2.
Reduction of Thiolate-Incorporated M^{II} Bis(imino)pyridine Complexes

Scheme 3.
Synthesis of the Mono-Reduced Complex $[Fe(LN_3S)(DMAP)]^0$ (4)

Table 1

Selected Bond Distances (Å) for $[Fe(LN_3S)]^{n+}$ Complexes

	$[Fe^{II}(LN_3S)(OTf)]^a$	$[Fe^{II}(LN_3S)(py)]OTf$	$[Fe^{II}(LN_3S)(DMAP)]OTf$	$[Fe^{II}(LN_3S)(DMAP)]^0$
Fe1–N1	2.188(2)	2.173(5)	2.1859(15)	1.9255(15)
Fe1–N2	2.072(2)	2.090(5)	2.0960(14)	1.8278(15)
Fe1–N3	2.184(2)	2.196(5)	2.2179(15)	1.9179(16)
Fe1–N4	N/A	2.073(5)	2.0667(14)	2.0508(16)
Fe1–S1	2.2942(8)	2.3246(18)	2.3295(5)	2.2179(5)
Fe–O1	2.0870(18)	N/A	N/A	N/A
N1–C7 (imine)	1.293(3)	1.298(8)	1.292(2)	1.347(2)
C7(imine)– C9(ipso)	1.480(4)	1.485(9)	1.486(2)	1.432(3)
C9(ipso)–N2(pyr)	1.343(3)	1.342(8)	1.341(2)	1.376(2)
N3–C14(imine)	1.284(3)	1.275(7)	1.290(2)	1.341(2)
C14(imine)–C13(ipso)	1.483(4)	1.494(8)	1.487(3)	1.426(3)
C13(ipso)–N2(pyr)	1.334(3)	1.334(8)	1.343(2)	1.381(2)

[a] Ref 24

Table 2

Selected Bond Angles (°) for $[Fe(LN_3S)]^{n+}$ Complexes

	$[Fe^{II}(LN_3S)(py)]OTf$	$[Fe^{II}(LN_3S)(DMAP)]OTf$	$[Fe^{II}(LN_3S)(DMAP)]^0$
N4–Fe1–N2	109.79(19)	112.91(6)	99.92(6)
N4–Fe1–N1	95.3(2)	99.69(6)	95.84(6)
N2–Fe1–N1	74.0(2)	73.08(5)	81.26(7)
N4–Fe1–N3	99.29(19)	99.82(6)	99.88(6)
N2–Fe1–N3	73.4(2)	73.94(6)	80.65(7)
N1–Fe1–N3	147.24(19)	146.17(5)	157.78(7)
N4–Fe1–S1	106.05(15)	107.20(4)	105.25(5)
N2–Fe1–S1	138.08(14)	135.18(4)	153.58(5)
N1–Fe1–S1	81.79(15)	81.40(4)	88.27(5)
N3–Fe1–S1	121.28(13)	118.28(4)	102.49(5)

Table 3

Selected Bond Distances (Å) and Angles (°) for Complex 5

	distance (Å)		angle (°)
Ni1–N1	1.8981(15)	N2–Ni1–N1	83.56(6)
Ni1–N2	1.8151(14)	N2–Ni1–N3	82.44(6)
Ni1–N3	1.9159(15)	N1–Ni1–N3	165.91(6)
Ni1–S1	2.1386(5)	N2–Ni1–S1	175.17(5)
N1–C7 (imine)	1.312(2)	N1–Ni1–S1	91.64(5)
C7(imine)–C9(ipso)	1.480(2)	N3–Ni1–S1	102.37(5)
C9(ipso)–N2(pyr)	1.341(2)		.
N3–C14(imine)	1.299(2)		
C14(imine)–C13(ipso)	1.480(2)		
C13(ipso)–N2(pyr)	1.338(2)		

Table 4

^{57}Fe Mössbauer Parameters for Selected High-Spin Iron(II) Complexes

	(mm s^{-1})	E$_Q$ (mm s^{-1})	Ground State (S)	Reference
[Fe^{II}(LN$_3$S)(DMAP)](OTf) (**3**)	0.87	2.70	2	This work
[(^{iPr}BIP)FeCl$_2$]	0.89	2.40	2	39
[(^{iPr}BIP)FeCl$_2$]	0.92	2.40	2	This work
[(^{iPr}BIP)Fe(SPh)Cl]	0.78	2.62	2	This work
[(^{Mes}BIP)FeCl$_2$]	0.90	1.12	2	80

Table 5

^{57}Fe Mössbauer Parameters for Mono- and Doubly-Reduced BIP-Iron Complexes

	δ (mm s^{-1})	E_Q (mm s^{-1})	S_{total}	S_{Fe}	S_{ligand}	Reference
Mono-reduced complexes						
[Fe^{II}(LN$_3$S)(DMAP) (**4**)	0.33	2.04	½	1	½	This work
[(^{iPr}BIP)Fe(CO)$_2$](BAr$^F_4$)	0.17	0.62	½	½	0	37
[(^{iPr} BIP)Fe(OEt$_2$)](BAr$^F_4$)	1.13	2.51	3/2	2	½	38
[(^{iPr}BIP)FeCl]	0.77	0.73	3/2^c	2	½	39
Doubly-reduced complexes						
[(^{iPr}BIP)Fe(DMAP)]	0.31	1.94	0	1	1	39
[(^{iPr}BAP)Fe(DMAP)]	0.30	2.04	0	1	1	82
[(^{iPr}BIP)Fe(CO)$_2$]	0.03	1.17	1	0	1	39, 82

BAP = bis(aldimino)pyridine